University of Canterbury

Department of Mathematics and Statistics
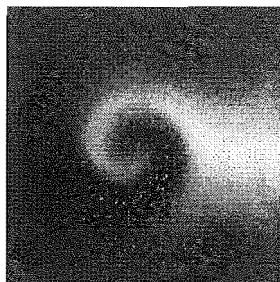
# Modelling Spiral Waves
# In Xenopus Laevis Oocyte

---

A thesis submitted in partial fulfilment
of the requirements of
the Degree for
Master of Science in Mathematics
at the
University of Canterbury
by
Andy McKenzie

---

Supervisor: Dr James Sneyd
1997

# Contents

# List of Figures

# List of Tables

# Abstract

An investigation was made into the spiral waves solutions for the Atri *et al* model, a partial differential equation model for $Ca^{2+}$ dynamics in the Xenopus laevis oocyte. Spiral wave solutions, both stable and unstable, were found to exist in the oscillatory regime for this model. The spiral wave solutions were found to have a period that decreased as the initial $IP_3$ bolus increased. Increasing the initial $IP_3$ bolus also lead to destabilisation of the spiral waves solutions. After the break up of spiral wave solutions complex spatio-temporal patterns occurred. In some cases spirals reformed after breaking up.

# Acknowledgements

# 1  Introduction

## 1.1  Overview

$Ca^{2+}$ plays an important role in the biology of animals. Most noticeably it is a major component of bones in the form of calcium phosphate. Less obvious are the important roles it has at the cellular level. At this level it functions as a signalling agent for a variety of cellular processes such as chemical secretion, cell division, and cell movement. However, while it is clear that $Ca^{2+}$ is a causal agent in these processes, the exact mechanisms by which it acts are not clear.

An important recent development is the observation that $Ca^{2+}$ forms a variety of complex spatial-temporal patterns inside cells. It is suspected that these patterns may convey information that control the nature of subsequent cellular processes. Therefore it is very important to understand how these patterns form. Experimental work has uncovered the basic mechanisms that lead to $Ca^{2+}$ oscillations, but the mechanisms involved are complex and the details are unclear. Because of this it has been necessary to build mathematical models to help understand the mechanisms involved, and to suggest further ideas for experimental research.

Spiral waves are a vivid example of the type of spatial-temporal patterns that may be observed inside cells. Spiral waves have a variety of characteristics such as a rotation rate and arm width. As a test of a mathematical model, the spirals that are produced may be compared to those observed experimentally. If the model spirals are similar to those observed experimentally then this suggests that the mechanisms postulated in the mathematical model are sufficient to produce the observed spatio-temporal patterns.

Atri *et al* have developed a mathematical model of $[Ca^{2+}]$ oscillations in Xenopus laevis oocyte based on the known biological mechanisms [2]. This model successfully reproduces many known experimental results. The model also produces circular, planar, and spiral waves. The aim of this thesis is to investigate in more detail the nature of the spiral waves that occur in this model. In particular are the spirals that form in the model unique, or do they differ in some essential characteristics such as rotation rates and arm widths? And on a more general level are the spirals that form in the model stable or not, and how does the stability depend on the initial conditions, boundary conditions, and parameter values?

## 1.2  Preview

Spiral waves are observed in many chemical and biological systems. In the following section (Section 1.3) the presence of spiral waves in the Belousov-Zhabotinskii (BZ) reaction, aggregation phase of the slime mould, and in heart abnormalities is

introduced. Recent research has found that spiral waves also occur in the Xenopus laevis oocyte (Section 1.4). While the patterns that occur in these disparate cases are very similar the actual mechanisms involved are very different. In order to make a model for Xenopus laevis that gives spirals waves *and* accurately reflects the actual mechanisms involved a detailed knowledge of the Xenopus laevis oocyte and its biochemistry is needed. In Section 2 the relevant biochemicals are introduced and in Section 3 the structure of a typical animal cell is outlined. Extensive experimental research has uncovered many of the roles of $Ca^{2+}$ inside a cell, and the mechanisms by which its concentration is controlled (Section 4). Based on these mechanisms a partial differential equation model may be developed for calcium waves in the Xenopus laevis oocyte (Section 5). These equations can not be solved analytically so must be solved by using numerical methods (Section 6). These equations can be solved to give stable spiral wave solutions (Section 7). However, for other parameter values and initial conditions unstable spirals result (Section 8). The unstable spirals break down to form complex spatio-temporal patterns. A transition from stable to unstable spirals can be induced by varying the size of one of the initial conditions (Section 9). The main results from these simulations are summarised in Section 10.

## 1.3   Spiral Waves in Biology and Chemistry

Spiral patterns have been observed in many biological and chemical systems. The most thoroughly investigated chemical system that produces spiral waves is the Belousov-Zhabotinskii (BZ) reaction [36], [37], [59]. The basic mechanism for this reaction consists of the oxidation of malonic acid by bromate ions $(BrO_3^-)$. This reaction is catalysed by cerium which takes the states $Ce^{3+}$ and $Ce^{4+}$ in solution. It is found that the concentrations of $Ce^{3+}$, $Ce^{4+}$, and $Br^-$ oscillate for long periods of time. The use of marker dyes allows this to be observed as a visual pattern in a dish. The BZ reaction is, relative to many biochemical reactions, a simple one. This has made it important as a model system for the application of reaction-diffusion equation models. Among the many spatiotemporal patterns this systems exhibits is spiral waves (Figure 1a).

Spiral waves are also found in the aggregation phase of the life cycle of the cellular slime mould *Dictyostelium discoideum* [56], [13]. The life cycle of the slime mould passes through the stages of spore-bearing stalk, spore, individual amoeba, aggregate, and finally slug. The slug moves to a place of warmth and light where it transforms into a spore-bearing stalk. The life cycle then starts all over again. The aggregation phase is initiated by a shortage of food. Aggregation centres form towards which individual amoeba cells migrate. Cells near an aggregation centre advance towards it, and at the same time release cyclic AMP from their posterior

end. The cells behind the advancing ones head towards a region of high cyclic AMP concentration, and also release cyclic AMP from their posterior ends. Pulsating wavelike patterns of motion result. One interesting pattern that can form is spiral waves (Figure 1b).

In normal circumstances the heat muscles, in a coordinated action, pump at a rate of 60 to 100 beats per minute. However sometimes this rhythm is disrupted and the irregularities in heart function called tachycardia and fibrillation can occur. Tachycardia is characterised by an abnormally fast heart beat, and fibrillation by a heart beat that is highly irregular in both amplitude and frequency. Both of these conditions, if they persist, can lead to death. Recent research indicates that the precursor to the both of these conditions is the formation of a spiral wave, or multiple spiral waves of electrical activity in the heart [17], [31].
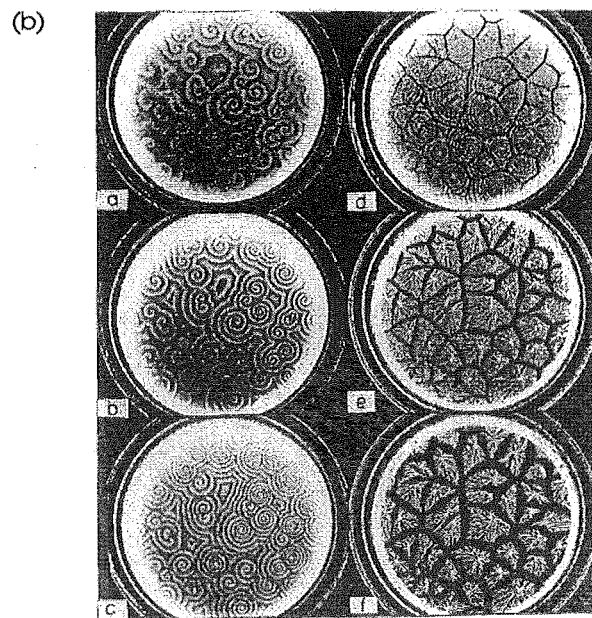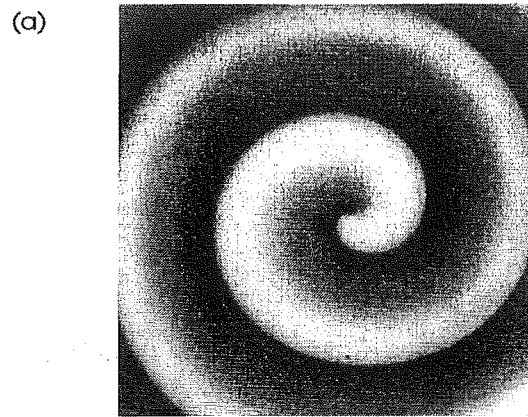
Figure 1: Spiral waves observed in biology and chemistry. (a) The Belousov-Zhabotinskii (BZ) chemical reaction. A spiral wave in a 1mm layer of BZ reactant. The grey scale image measures the intensity of transmitted light. This corresponds to isoconcentration lines for one of the reactants [35]. (b) The aggregation phase of the slime mould Dictyostelium discoideum. The slime mould are in a Petri dish which is 50mm in diameter, of which photographs were taken about every 10 minutes. Moving and stationary cells have different optical properties under illumination. Moving cells are bright and stationary cells are dark [39].

## 1.4 Spiral Waves in Xenopus Laevis Oocyte

### 1.4.1 Introduction

*Xenopus laevis* is a species of frog that is native to sub-Saharan Africa. The genus Xenopus contains approximately 20 species,of which Xenopus laevis is one of them [24]. Xenopus has the latin meaning "peculiar foot", while laevis means "smooth". The common name for Xenopus laevis is the African Clawed Frog or the Upland Clawed Frog.

Xenopus laevis is a primitive frog that has not changed its appearance in 125 million years. It has four long unwebbed front fingers, and five webbed back fingers with claws on three of them. Its body is flattened with eyes on top, and an olive gray coloured skin. Unlike other frogs it lacks ears, eyelids or a tongue.

The frog was brought to the U.S.A. in the 1950s where it was used to diagnose pregnancies; the female frog lays eggs when injected with the urine of a pregnant woman [24]. It was released from captivity and has now established itself in the streams and ponds of the American Southwest. It has established itself so well that it is now something of a threat to native frogs.

Xenopus laevis is popular as an experimental animal because it can tolerate a wide variety of living condition [62]. It is well adapted for brackish water, and can handle extremes of pH. This makes it an easy and inexpensive animal to maintain.

### 1.4.2 Xenopus Laevis Oocyte

An oocyte is an immature female egg cell. It is one of the stages in the development of an embryo and precedes fertilisation. After fertilisation the egg cell reproduces to form a large mass of cells. These cells segregate into distinct units which later form internal organs. Eventually after a number of complex and highly integrated processes a fully formed organism develops.

The ovary of a female Xenopus Laevis contains thousands of oocytes. These take 6 to 8 weeks to mature. By convention the maturation process is divided into six stages (I-VI). It is the Stage V and Stage VI eggs from albino frogs that are used in experiments [30]. Albino eggs are more transparent than other eggs, so their internal structure is more easily revealed using microscopy techniques.

The oocytes of Xenopus Laevis are particularly easy to obtain. An advantage for experimental work is that they are also very large cells (up to 1.3mm in diameter). Xenopus Laevis oocytes have proved to be popular as manufacturing systems for the structures encoded by messenger RNA from other organisms. They have been used to produce the proteins encoded by foreign messenger RNA, and to express foreign receptors or ion channels on the plasma membrane [16].

### 1.4.3 Confocal Fluorescent Microscopy of Oocytes

Confocal fluorescent microscopy is a technique that can be used to investigate calcium concentration in cross-sections of an oocyte. This technique combines the technology of confocal microscopy with the use of fluorescent dyes to mark the distribution of $Ca^{2+}$.

Confocal microscopy is a technique for imaging light that comes from a single cross-section [16]. Light from surrounding cross-sections is out of focus, so is not imaged. This is an invaluable technique as it enables a living oocyte to be imaged at different depths. This is much harder to do with conventional microscopy which combines the light from all the sections of an imaged object. Typically a sequence of images is taken of a cross-section. These may then be combined to give a frame by frame animation showing how the $[Ca^{2+}]$ changes in the cross-section.

Fluorescent dyes bind $Ca^{2+}$, with a resulting change in the spectrum of the light they emit. Depending on the experimental setup, an excitation or emission spectrum can be measured for a dye. An excitation spectrum is found by measuring the intensity at a fixed wavelength, while excitation light is scanned through out the wavelengths. The intensity of the emitted light is plotted versus the excitation wavelength to give an excitation spectrum. An emission spectrum is found by measuring the intensity over a wavelength range, while exciting at a fixed wavelength. Plotting the emission intensity versus the emission wavelength gives an emission spectrum. A spectrum, whether excitation or emission, has two main characteristics: (1) the intensity at different wavelengths and, (2) the wavelength at which maximum intensity occurs.

There are two types of dyes used for fluorescent microscopy: (1) quantitative ratiometric dyes, and (2) single visible wavelength dyes [12]. For ratiometric dyes the wavelength at which maximum intensity occurs changes upon the binding of $Ca^{2+}$. The ratio of the wavelength with $Ca^{2+}$ bound, and no $Ca^{2+}$ bound, can be used to determine the calcium concentration. The shift in the position of the maxima is independent of the dye concentration and the light pathlength. This is important as it can be difficult to set up a homogeneous distribution for indicator dyes, and light from different depths in a cell may need to be collected. The primary disadvantage of ratiometric dyes is that ultraviolet light must be used to excite them. This requires the use of more complex instrumentation for microscopy, precludes ratiometric dyes being used for cells that autofluoresce with ultraviolet light, and can not be used for experiments that use ultraviolet light to release compounds into the cell . Single visible wavelength dyes, upon binding $Ca^{2+}$, do not undergo a significant change in the wavelength at which maximum intensity is observed. However, the intensity of the emitted light increases, and this is proportional to the calcium ion concentration. The main advantage of single visible wavelength dyes is, as the name indicates,

that they need only visible wavelength light to excite them. Because of this the instrumentation required is cheaper and easier to use.

### 1.4.4 Experimental Data

Spatial-temporal patterns of $[Ca^{2+}]$ in Xenopus laevis oocyte have been observed using confocal fluorescent microscopy [29], [30] , [28]. Xenopus laevis oocyte is a convenient model system for investigating the mechanisms underlying calcium oscillations for a number of reason. Compared to other cell types the processes involved in calcium oscillations are simpler and therefore easier to study experimentally. Also the oocyte is a a large egg (up to 1.3mm in diameter). This makes it easier to use in experimental work, and it is large enough for complex patterns such as spirals for form.

A chemical central to the mechanisms involved in the production and mediation of calcium waves in Xenopus laevis oocyte is inositol trisphosphate $(IP_3)$ (see Section 4.3.3) The mechanisms for the production of $[Ca^{2+}]$ waves may be by-passed by directly controlling the $[IP_3]$ levels. A convenient procedure for doing this is to cage $IP_3$ in another compound, then release it from this compound using ultraviolet light. In this way the spatial distribution and time of release of the $IP_3$ may be controlled. The type of patterns observed in the oocyte include travelling waves, target patterns (circular waves propagating from a centre), and spiral waves.



t=0 s          t=6 s
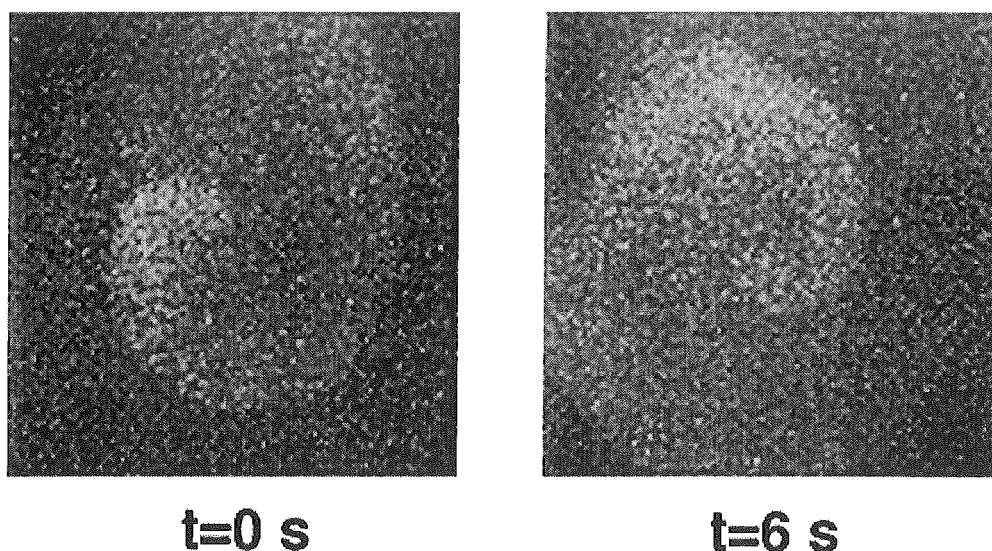
Figure 2: Spiral waves observed in Xenopus laevis oocyte [2].

# 2 Biochemistry

## 2.1 Introduction

It is at the level of biochemistry that cellular processes may be best understood. The biochemistry of cells is a vast and expanding subject area. The purpose of this section is to introduce specific biological molecules that play a role in the mechanisms underlying $[Ca^{2+}]$ oscillations.

## 2.2 Enzymes

Catalysts are chemicals that can increase the rate of a reaction without been used up themselves. Therefore they can be used in a reaction repeatedly, and only small amounts are required to keep a reaction going. They work by lowering the activation energy of a reaction. An example of a inorganic catalyst is platinum. In the form of a finely ground powder it catalyses a reaction between $H_2$ and $O_2$ with explosive effects.

Enzymes are biological catalysts [57] ,[6]. They consist of large globular proteins, and can increase the rate of a biological reaction up to a million fold or more. Without enzymes the molecules on which enzymes act would retain their stable structures for long time, to long to be biologically useful.Therefore enzymes allow organisms to retain molecules with stable structures, but to change these structures when required. Enzymes are also very specific in their action. A given enzyme can usually act on only one compound or pair of compounds. However, the use of enzymes comes at a cost as it requires a great deal of energy to manufacture enzymes.

The surface of an enzyme has a small area called an active site (sometimes there are many active sites). The active site is formed from amino acids from different parts of the enzymes that group together to give the site a particular shape. The shape of the site is complementary to the shape of substance(s) that the enzyme acts on, just like a lock and key have complementary shapes. It is this particular shape that makes the action of enzymes so specific.

Enzymes and reacting molecules do not just knock into each other and then react. Instead they form a complex held together by weak bonds, the enzyme-substrate (ES) complex. The enzyme and substrate shapes are complementary hence they fit together tightly which allows weak bonds to form between them. Sometimes after binding the enzyme changes shape to improve the fit even more. Subsequently catalysis takes place resulting in the formation of products and the original enzyme (Figure 3).
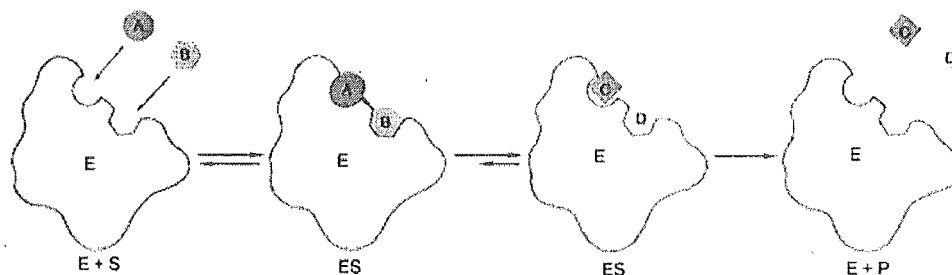
Figure 3: The basic mechanism for enzyme action. The reactants A and B fit into active sites on the enzyme that are complementary to the shapes of the reactants. The enzyme and reactants then form an enzyme-substrate (ES) complex. The reactants are converted to the products C and D and are released from the active sites. The enzyme is now free to catalyse another reaction [58].

## 2.3 Phospholipids

Phospholipids are members of the lipid family. The lipid family includes fats, oils, and steroids. They all share the common property of being insoluble in water.

The characteristic structural member of a phospholipid is a group called glycerol phosphoric acid (Figure 4). This group contains the charged phosphate group $PO_4^{3-}$, which makes one end of a phospholipid polar. This end is attracted to the polar water molecule, and is described as hydrophilic ("water loving"). The other end has two long fatty acid chains and is hydrophobic ("water hating"). Thus one end of a phospholipid is hydrophilic and the other end is hydrophobic. This induces a phospholipid to spontaneously form a spherical layer in a water solutions [8]. This property is important for the formation of cellular membranes, of which phospholipids are a major component.

## 2.4 The Energy Molecules: ATP and GTP

Adenosine Triphosphate (ATP) and Guanosine Triphosphate (GTP) are the fuel for a wide variety of processes inside a cell. Both contain three high energy phosphate groups. When one or more of these phosphate groups splits from the molecule energy is released. This released energy is stored in other molecules, which then power biological processes. ATP is by far the most common of these two molecules and powers a variety of biological processes such as the building of high energy molecules, cell division, cell movement, and the transport of ions across cell membranes. GTP is not as common, but is important in the mechanisms involved in the formation of calcium waves.
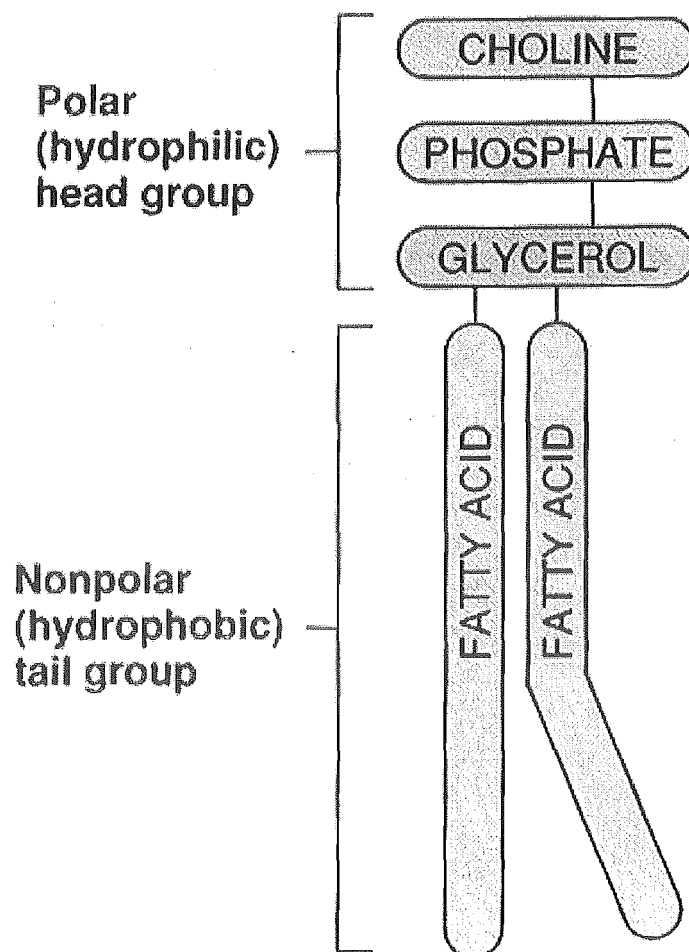
Figure 4: A typical phospholipid. One end contains the polar phosphate group, while the other end contains two nonpolar fatty acid chains. This particular phospholipid contains the group choline and hence is called phosphotidylcholine.

# 3 Animal Cells

## 3.1 Introduction

A schematic of a typical animal cell is shown in Figure 5. As can be seen from the figure there are many parts to an animal cell. These parts have many functions such as the formation of high-energy compounds (mitochondria), protein synthesis (ribosomes), digestion and waste disposal (lysosomes), storage of genetic material (nucleus), and cell movement (cilium). With regard to the production of calcium waves experimental evidence indicates that most of these parts may be neglected. The structures that are involved in the production of calcium waves are the endoplasmic reticulum, cytoplasm, and the plasma membrane.
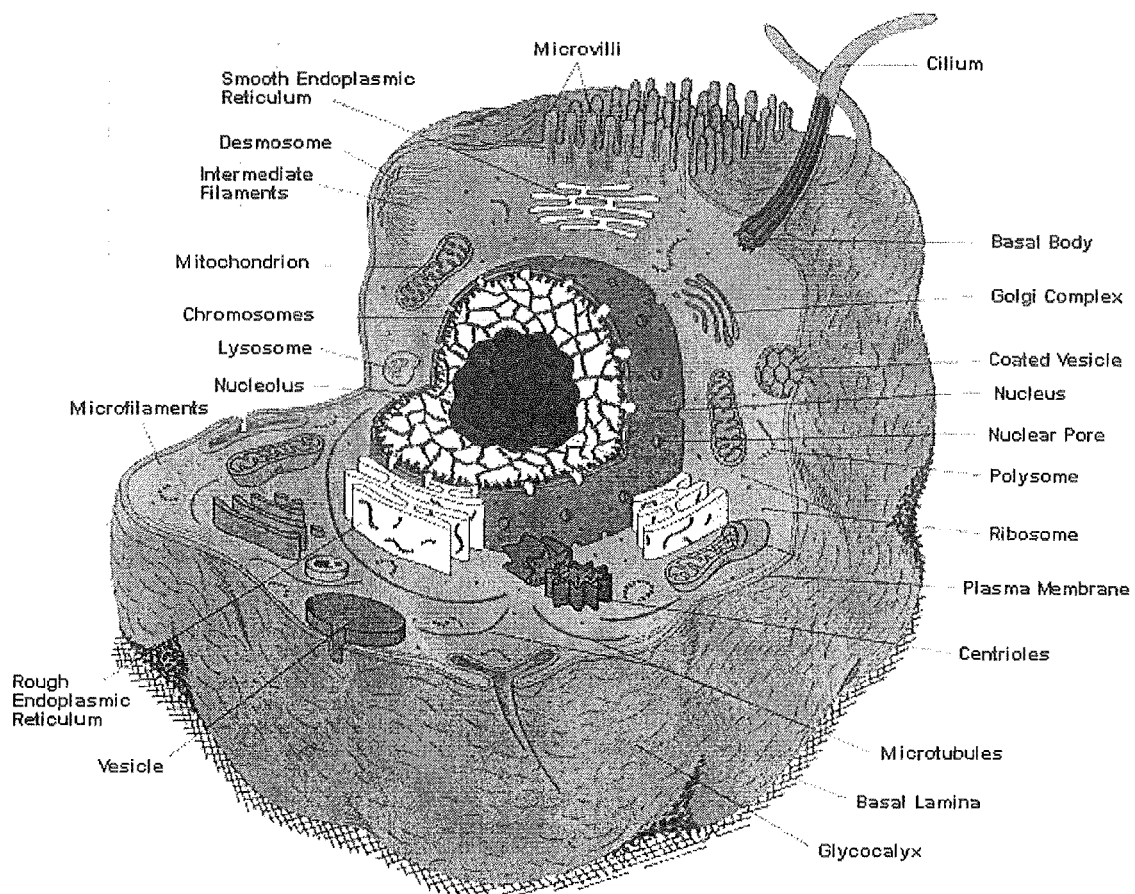


Figure 5: A typical animal cell.

## 3.2   Endoplasmic Reticulum

The endoplasmic reticulum (ER) was discovered in the 1950s. There are two types of ER: the rough ER (RER) which is studded with ribosomes, and the smooth ER (SER) which is not. The ER is the place where proteins for export or for special sites in the cell are made and modified.

The RER is the site of protein synthesis (Figure 6). Polysomes, the active units producing proteins attach to the RER membrane at membrane receptors. Here the protein is synthesized and passed into the channels between the RER membranes called cisternae. Once in the cisternae the proteins are transported to other sites for storage, export, or modification.
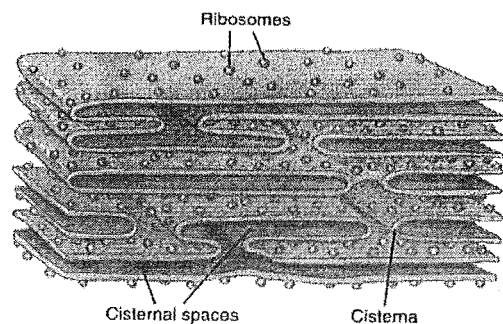


Figure 6:  The rough endoplasmic reticulum (RER). The ribosomes are sites of protein synthesis.

The SER is an intermediate transport path between the RER and an organelle called the Golgi complex. The SER and its associated enzymes are involved in transportation, synthesis, and metabolism (chemical modification) of small molecules. It is abundant in cells that synthesise fats and steroids. For example, in ovaries and testes the SER is the site of production of steroid sex hormones. In certain cell types the SER contains enzymes that oxidise toxic substances. The enzymes make other molecules more polar, hence they are excreted from the cell and body more quickly. The SER has specialised functions in certain cell types. For example, in liver cells the SER contains enzymes that help to modify glucose so that it passes through the SER, thereby enabling it to be transported to the cell surface and needy cells in the body. The SER is important in muscle cells. It contains calcium ions which are released when muscle cells are stimulated by a nerve impulse. The calcium ions trigger the contraction of muscles.

Of particular interest, with regard to $[Ca^{2+}]$ oscillations, is that the ER is one of the sites of intercellular $Ca^{2+}$ storage [53]. $Ca^{2+}$ pumps bring $Ca^{2+}$ into the ER where it binds to buffer proteins such as calsequestrin. Little is known about how the calcium storage sites in the ER are connected. Because the ER has a highly convoluted structure it is possible that the storage sites in the ER are localised structures. Therefore there would be little diffusion between the storage sites. It has also been suggested that maybe the intercellular storage site for $Ca^{2+}$ is a specialised component of the ER organelle, or perhaps another organelle altogether given the name the "calciosome" [54]. However there has been little further evidence to support this claim.

## 3.3 Plasma Membrane

### 3.3.1 Introduction

The plasma membrane is the name given to the membrane that surrounds a cell. The main structural component of the plasma membrane is a bilayer of phospholipids. One end of a phospholipid molecule is hydrophobic, and the other end is hydrophilic. Because of this in a water solution the phospholipid molecule orientates itself so that the hydrophilic head is on the outside, and the hydrophobic tail is on the inside (Figure 7). This bilayer is not a rigid structure; the lipid molecules are not tightly bound together, and the two layers can easily slide over each other.
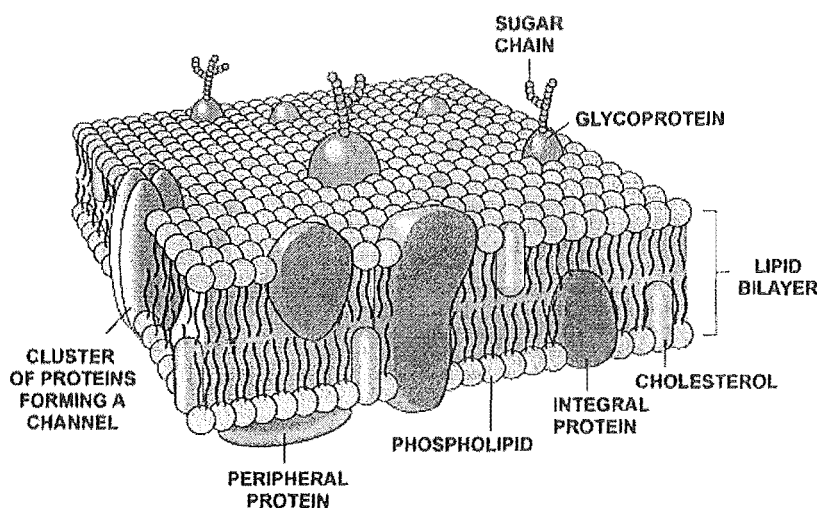


Figure 7: The plasma membrane. Phospholipids are a major component of the plasma membrane.

Floating within the membrane are various proteins. One function of certain types of these proteins is to transport molecules across the cell membrane.

These proteins function as carriers or pumps of other molecules. Other proteins, those more near the outer surface, function as marker tags for the attachment of other molecules. These type of proteins are called receptors. A special class of proteins called G-proteins is found more toward the inner surface of the membrane. G-proteins function as intermediate chemical messengers between a receptor and intracellular processes. All these proteins take part in the process that results in calcium waves. Further details of their structure and role are outlined in the following sections.

### 3.3.2  Transport Processes

As part of the metabolic process of life a cell needs to bring nutrients into the cell, or pass wastes out of the cell. All these nutrients or wastes must pass through the plasma membrane. Because the materials that need to be transported have different chemical structures and sizes a number of different transport mechanisms are used by a cell. Transport mechanism are of two types: passive transport which does not use up energy, and active transport which does.

The inner layer of the membrane lipid bilayer is hydrophobic and therefore will not allow charged ions or proteins to pass through it. However, molecules that are soluble in lipids may pass through the membrane by a process called diffusion. Diffusion occurs when there is a difference between the concentration of a molecule on the inside and outside of the cell membrane. When there is a difference in concentration then molecules will move from the region at high concentration to the region at low concentration.The greater the difference in concentration the greater the rate of diffusion.

A process by which substances can be moved faster across the membrane is carrier-facilitated diffusion. A molecule that can not, by itself, diffuse across the membrane can attach to one that can (the carrier). When the carrier has passed through the membrane the molecule is released. This process, like simple diffusion, is an example of passive transport and does not involve any energy expenditure by the cell.

However, even for large concentration differences, the rate of diffusion is very small. Passive diffusion, by itself, does not move molecules at a fast enough rate to keep up with the metabolic processes of a cell. In addition diffusion can only move substances from regions of high concentration to regions of low concentration.

Active transport mechanisms require the input of energy from the cell, but can move substances across the membrane from a region of low concentration to a region of high concentration. The transport mechanism consists of an assemblage of protein molecules that span the membrane. This assemblage is referred to as a pump. The source of energy for many pumps is the splitting of ATP into ADP. The

enzymes involved in this are referred to as ATPases, and hence a pump powered by ATP is referred to as an ATPase pump.

Calcium pumps are important for maintaining low intercellular $[Ca^{2+}]$ levels. The $[Ca^{2+}]$ outside a cell is about 20,000 times the intercellular concentration [9]. Without the pumping of $Ca^{2+}$ out of the cytoplasm by calcium pumps the intercellular $[Ca^{2+}]$ would quickly rise due to passive diffusion. If the intracellular $[Ca^{2+}]$ becomes too high then a cell dies.

### 3.3.3 Receptors

Receptors are proteins, most of which span the plasma membrane [14]. They help to convert an external signal (e.g. light, hormone, or neurotransmitter) into internal cell processes. The activation of a receptor initiates a sequence of chemical reactions in the plasma membrane, such as the activation of G-proteins. The activation of receptors is very specific. Only very specific chemical structures will activate a receptor, and the subsequent cellular processes.

### 3.3.4 G-Proteins

G-proteins are a class of proteins that can bind guanine nucleotides (such as GTP), and use the energy contained within the nucleotide to change their configuration [34]. This affects the ability of the protein to activate enzymes. The importance of G-proteins is that they are intermediaries in a multitude of receptor-activated events. Because of this intermediary status they are important in determining the effectiveness and sensitivity of signalling events.

Experimental evidence indicates that G-proteins are embedded on the inner side of the plasma membrane. Structurally a G-protein has three subunits, the $\alpha, \beta$ and $\gamma$ subunits. The $\alpha$ subunit determines the function and specific action of the G-protein. The $\beta$ and $\gamma$ units are very similar across all G-proteins. Upon activation by a receptor GTP binds to the $\alpha$ subunit. The $\alpha$ subunit, along with the bound GTP, dissociates from the G-protein. It diffuses through the cytosol where it activates enzymes that are attached to the inner side of the plasma membrane. After enzyme activation the $\alpha$ subunit reattaches to the $\beta$ and $\gamma$ subunits.

## 3.4 Calcium Binding Proteins

Dissolved within the cytoplasm and ER are a variety of nutrients, soluble proteins, and enzymes. Some of these soluble proteins bind $Ca^{2+}$ so are important for mediating $[Ca^{2+}]$ levels, and act as intermediaries for $Ca^{2+}$-induced changes in cell processes. It is convenient to divide calcium binding proteins into two types: buffer proteins, and trigger proteins [19].

Trigger proteins set off other reactions upon the binding of $Ca^{2+}$. A trigger protein that is common in the cytoplasm is calmodulin (*calcium-modulating protein*). Calmodulin changes shape upon the binding of $Ca^{2+}$, for which it has four binding sites. When calmodulin changes shape it binds more easily to various regulatory target proteins, resulting in the activation of enzymes and the opening of ion channels.

Buffer proteins simply bind $Ca^{2+}$ without setting off any further chemical reactions. The ER uses the buffer protein calsequestrin as a repository for $Ca^{2+}$ brought into the ER by $Ca^{2+}$ pumps. The cytoplasm also contains buffer proteins, but little is known about their characteristics or buffering capacity. Moreover, it is likely that the type of buffer proteins found in the cytoplasm differ between cell types. However, in chromaffin cells it is known that approximately 98 percent of the $Ca^{2+}$ that enters the cytoplasm is bound by buffer proteins [38]. This indicates that the cytoplasm is very highly buffered. Buffering, along with $Ca^{2+}$ ATPase pumps, helps to keep the intracellular $[Ca^{2+}]$ low.

# 4   The Role of $Ca^{2+}$

## 4.1   Effects of $Ca^{2+}$

$Ca^{2+}$ has widespread effects throughout a cell. It is implicated in processes as diverse as chemical secretion, muscle contraction, gene expression, cellular growth, and enzyme activation [9], [53], [30]. However, while it is clear that $Ca^{2+}$ is a causal agent in these processes the detailed mechanisms by which it acts is not clear.

A clear example of the action of calcium occurs in the fertilisation of an egg cell by sperm [18]. When a sperm enters the egg a calcium wave spreads throughout the outer layer of the egg. This calcium wave activates processes which cause the membrane of the egg to harden. As a result of this no further sperm may enter the cell.

As had been indicated a change, in $[Ca^{2+}]$ is a precursor to many cellular events. Of potentially even more importance is the discovery that $[Ca^{2+}]$ levels also *oscillate*. The frequency of the oscillations may convey extra information that influences subsequent cellular processes.

## 4.2   Effects of $Ca^{2+}$ Oscillations

Numerous plausible, but speculative hypotheses, have been suggested for the role of $[Ca^{2+}]$ oscillations inside a cell. It is apparent that more experimental evidence is needed to determine what function, if any, $[Ca^{2+}]$ oscillations do have.

In high enough concentrations $Ca^{2+}$ will kill a cell. One role of calcium pumps and calcium buffering proteins is to keep the cytoplasmic levels of $[Ca^{2+}]$ low. Typically the extracellular cytoplasmic $[Ca^{2+}]$ is 20,000 times higher than the intracellular $[Ca^{2+}]$ . Calcium waves allow $[Ca^{2+}]$ to reach high enough levels to activate a process, but as the elevation of $[Ca^{2+}]$ is only temporary the wave is not toxic in its effects.

A related hypothesis is that information is somehow encoded in the frequency of the $[Ca^{2+}]$ waves [53]. So in addition to counteracting toxic effects, a wave could convey information throughout the cell. The advantage of using the frequency to encode information is that the frequency of a wave is not easily disrupted, unlike the wavelength or amplitude. Therefore frequency encoded information has a low noise-signal ratio. The sort of information encoded in the frequency might include the amount surface membrane receptors have been activated by hormones or neurotransmitters. A clear example of this effect is in vasopressin-induced $[Ca^{2+}]$ oscillations in a liver cells from a rat. The higher the concentration of the hormone that the cell is exposed to, the greater the frequency of the $[Ca^{2+}]$ oscillations (Figure 8). Note that the amplitude of the oscillations remains the same.
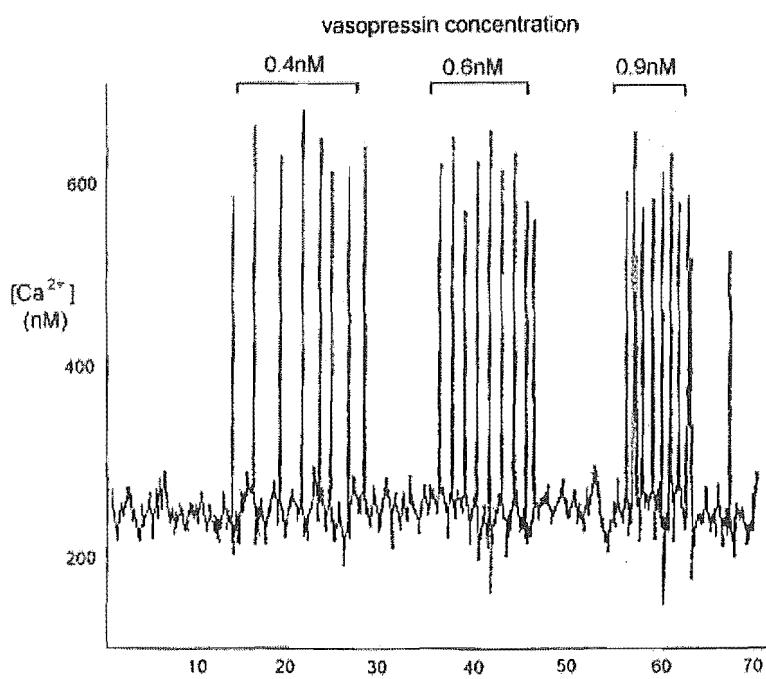
Figure 8: Vasopresin-induced oscillations in a rat live cell. The higher the concentration of vasopressin the greater the frequency of the oscillations. The amplitude of the oscillations remains the same [61].

## 4.3 The Biological Mechanism for Calcium Waves

### 4.3.1 Introduction

There is not a single mechanism by which cells control their cytosolic calcium concentration. Instead a variety of membrane pumps, membrane channels, internal stores, and feedback mechanisms are used. These differ from cell type to cell type. However it is convenient to categorise cell into two types: excitable and nonexcitable. These two types of cell differ in the basic mechanisms they use to control cytosolic calcium concentration.

Nonexcitable cells, of which Xenopus laevis oocyte is an example, share the same basic mechanisms for controlling cytosolic calcium concentration. However the details differ from cell type to cell type. These details include such things as the rate of flux through channels, pump strengths, and receptor sensitivities. An even more important difference is the presence of feedback in the chemical reactions that occur. A detailed biological model for calcium waves in Xenopus laevis oocyte must take all of these into account.

### 4.3.2 Excitable and Nonexcitable Cells

Due to the differing concentrations of ions such as $K^+$, $Na^+$, and $Ca^{2+}$ inside and outside a cell, all cells sustain a voltage potential difference across their cell membrane. Cells are categorised as either excitable or nonexcitable according to how they react to a perturbation to this membrane potential [25]. For nonexcitable cells the membrane potential, upon the removal of the perturbation, returns to its original state. Excitable cells, by contrast, react to a sufficiently large perturbation by a large change in their membrane potential before they return to their original state. This large change in membrane potential is called an action potential.

Nonexcitable cells increase intercellular $Ca^{2+}$ by releasing it from the ER , a process set in action by the activation of receptors on the ER. The activity of these receptors is modulated by both $IP_3$ and $Ca^{2+}$ (see below). The mitochondria, Golgi apparatus, and nuclear envelope are also believed to contribute to make a contribution to the cytosolic $[Ca^{2+}]$ flux, but the details of their contribution are unknown [50]. Examples of nonexcitable cells include blood cells, liver cells, and the Xenopus laevis oocyte.

In addition to the above described mechanism excitable cells also have voltage-gated $Ca^{2+}$ channels imbedded in the cell membrane. A change in the membrane potential opens a channel allowing $Ca^{2+}$ to cross the cell membrane and enter the cytoplasm. Because excitable cells have a greater number of mechanisms for changing the cytosolic $[Ca^{2+}]$ the experimental study of $Ca^{2+}$ flux in them is much harder. Examples of excitable cells include muscle cells and nerve cells.

### 4.3.3 Xenopus Laevis Oocyte

The cell Xenopus laevis oocyte, for which a mathematical model of $[Ca^{2+}]$ oscillations was constructed, is a nonexcitable cell. A pictorial outline of the processes thought to be involved in the production of calcium waves in Xenopus laevis oocyte is shown in Figure 9. Notice that, unlike some other nonexcitable cells, no ryanodine/$Ca^{2+}$ channel is present [41]. Further details of this process are outlined in the following.

A hormone or neurotransmitter binds to the receptor R. This stimulates GTP to replace GDP in the G-protein, inducing the $\alpha$ subunit to dissociate from the G-protein. The $\alpha$ subunit diffuses through the plasma membrane where it activates the enzyme phosphodiesterase (PLC). This enzyme catalyses the break up of phosphotidylinositol-(4,5)-bisphosphate ($PIP_2$) into inositol trisphosphate ($IP_3$) and diacylglycerol (DAG). Both $IP_3$ and DAG stimulate further cellular responses, but via different reaction pathways. $IP_3$ diffuses through the cell cytosol where it activates receptors located on the endoplasmic reticulum (ER). This brings about the release of $Ca^{2+}$ from the ER.

The basic details of the processes involved in calcium oscillations in Xenopus laevis, as outlined above, are agreed upon. What is not agreed upon are the details of the process, in particular what feedback is present. A basic area of disagreement is whether or not $[IP_3]$ oscillations are essential for calcium oscillations. Most models that incorporate oscillations in $[IP_3]$ do so by including feedback on the production of $IP_3$. [33],[10]. The feedback causes $[IP_3]$ to oscillate, which in turn drives oscillations in $[Ca^{2+}]$ . However, experiments with the nonmetabolisable myoinositol (1,4,5)trisphosphorothioate ($IP_3S_3$), instead of $IP_3$, indicate that calcium oscillations can occur at constant $[IP_3]$. This has been confirmed for the Xenopus laevis oocyte [30] and a variety of other cell types [42],[55]. Therefore for calcium oscillations to occur in the Xenopus oocyte a feedback mechanism that leaves $[IP_3]$ constant must be present. In the Atri et al model $Ca^{2+}$ release from the IPR is modulated by $[Ca^{2+}]$ ; the release is less at low and high $[Ca^{2+}]$ , but more at intermediate $[Ca^{2+}]$ . A number of other different feedback mechanisms have also been postulated [51],[11].

$IP_3$ and $Ca^{2+}$ are not immobile but diffuse throughout the rest of the cytosol inducing further release of $Ca^{2+}$. Released $Ca^{2+}$ simultaneously diffuses through the cell membrane and ER membrane, and is pumped into the ER and pumped out of the cell. $IP_3$ is metabolised via complex pathways into a variety of other inositol phosphates whose function in many cases is unknown [44].
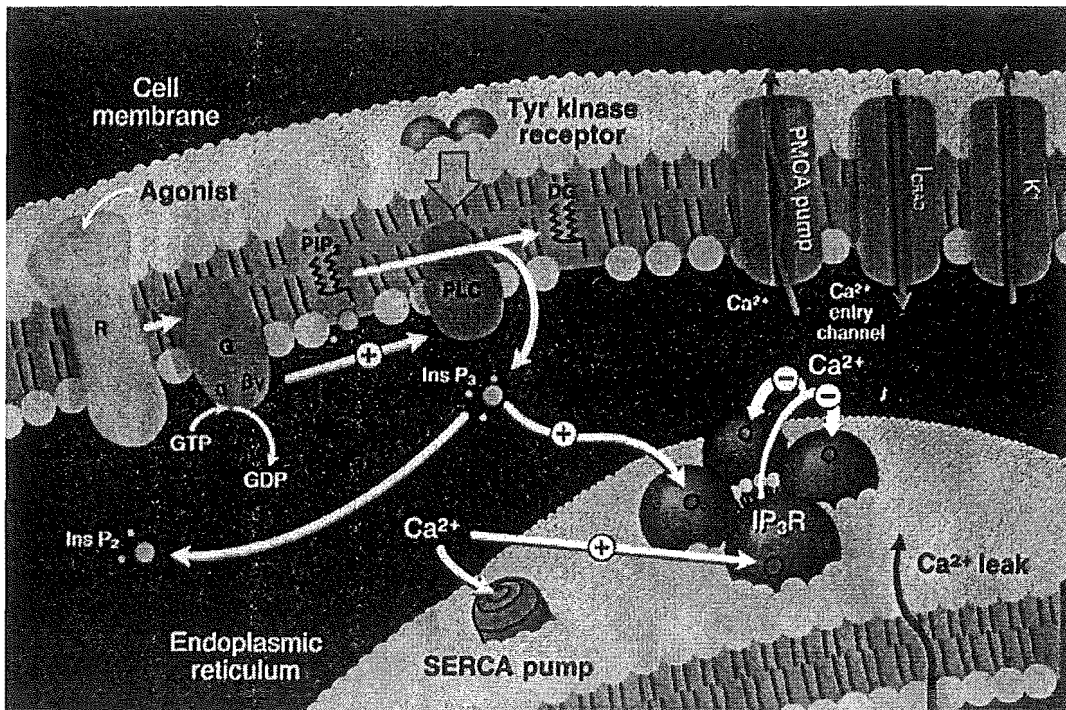
Figure 9: The biological mechanism for $[Ca^{2+}]$ oscillations [9].

# 5 Partial Differential Equation Model

## 5.1 Introduction

A partial differential equation model based on the biological mechanisms for the Xenopus laevis oocyte outlined in Section 4.3 was developed by [2]. The simplifying assumptions of homogeneity, continuity, and fast $[Ca^{2+}]$ buffering were made in the model. These assumptions were made, in part, to ensure that the model was not unnecessarily complicated. They also reflect the fact that when the model was constructed there was little experimental data available to enable the construction of a more detailed model.

Furthermore the partial differential equation model is in two dimensions instead of three dimensions. This is for two reasons. Firstly, and most importantly, the experimental data indicates that in the Xenopus Laevis oocyte the calcium wave activity is localised to a region near the surface of about $100\mu m$ thick [41]. Therefore, as an approximation, the calcium wave activity may modelled as a two-dimensional phenomenon. Secondly, from a practical perspective, it is computationally prohibitive to solve a three-dimensional model.

A mathematical analysis of the model equations without diffusion indicates that, depending on $[IP_3]$, the system may act as "nonexcitable", "excitable" or "oscillatory". The qualitative behaviour of the system to perturbations differs, depending on which of these three regimes it is operating in. The stability properties of spiral waves, which can form after a perturbation to the system, may depend on which of these three regimes the system is operating in.

## 5.2 Background to the model

### 5.2.1 Model Assumptions

The simplifying assumptions of homogeneity and continuity are made. Thus the mathematical terms modelling diffusion, pumping, and receptor activation do not have any spatial dependence (homogeneity). The continuity assumption smears out the discrete distribution of the $Ca^{2+}$ pumps and the IPR.

It is known that these modelling assumptions are not entirely correct . Experiments with the Xenopus laevis oocyte indicate that there are hotspots of calcium release activity [30]. These hotspots could be due to regions of higher IPR sensitivity or IPR density, both of which are violations of the homogeneity assumption. Furthermore the ER, the intracellular storage site for $Ca^{2+}$, does not have a homogeneous or continuous distribution. However, while the assumptions are known not to be entirely correct, they do accurately represent the essential features of the system . If data regarding inhomogeneities became available it could be incorporated

into the model, though this would not be easy.

Up to 98 percent of the $Ca^{2+}$ in the cytoplasm may be buffered by binding to proteins (Section 3.4). Essentially the buffering proteins act as another dynamic pool of $Ca^{2+}$. However little is known about the details of this buffering. If buffering is assumed to be fast then buffering effects may be modelled by scaling all $[Ca^{2+}]$ fluxes by a scalar [50]. For example, if 98 percent of $Ca^{2+}$ is buffered quickly then all $[Ca^{2+}]$ fluxes can be scaled by a factor of 0.02. The rescaled $[Ca^{2+}]$ represents the cytosolic concentration of unbound $Ca^{2+}$.

Buffering also lowers the diffusion coefficient of $Ca^{2+}$. Without buffering $Ca^{2+}$ has a diffusion coefficient of about $800\mu m^2 \cdot s^{-1}$ [9]. In a cytosolic extract from the Xenopus laevis oocyte the diffusion coefficient of $Ca^{2+}$ is much lower and depends on the concentration of $Ca^{2+}$ [1]. For typical $[Ca^{2+}]$ levels the diffusion coefficient takes on values between 15 and 65 $\mu m^2 \cdot s^{-1}$ . As the $[Ca^{2+}]$ increases the diffusion coefficient increases in a sigmoidal relationship. In the model the diffusion coefficient is taken as a constant, with a value of $25\mu m^2 \cdot s^{-1}$. Previous simulations indicate that including a $[Ca^{2+}]$ dependent diffusion coefficient has very little effect on the model behaviour [2].

### 5.2.2 The Equation for $[IP_3]$

$IP_3$ diffuses passively through the cytosol, while simultaneously breaking down into other inositol phosphates. The rate of diffusion is taked to be a constant, and a simple mathematical term is used to represent the degradation of $IP_3$. Therefore the equation for $IP_3$ is

$$\frac{\partial P}{\partial t} = D_p(P_{xx} + P_{yy}) - k_p P \tag{1}$$

where P is the $[IP_3]$, and $D_p$ and $k_p$ are constants.

### 5.2.3 The Equation for $[Ca^{2+}]$

$Ca^{2+}$ is assumed to passively diffuse through out the cytosol with a constant rate of diffusion. (see Section 5.2.1). $Ca^{2+}$ can enter or leave the cytosol in three ways: (1) it can be released from an IPR channel, (2) pumped out of the cytosol or (3) leak into the cytosol from the ER or through the cell membrane. Therefore the equation for the calcium concentration (c) is of the form

$$\frac{\partial c}{\partial t} = D_c(c_{xx} + c_{yy}) + J_{channel} - J_{pump} + J_{leak}. \tag{2}$$

The rate of release of $Ca^{2+}$ from the IPR channel depends on both $[IP_3]$ and $[Ca^{2+}]$ . A term for $J_{channel}$ was chosen that agrees with this, and also replicates the results obtained from experiments for which the pumping efflux was measured

as a function of the calcium concentration [41]. As a guide to understanding, the $J_{channel}$ term may be derived from a hypothesized physical model for the $IP_3$ receptor (Appendix A). In anycase the $J_{channel}$ term takes the form

$$J_{channel} = k_{flux}\mu(P)n\left(b + \frac{V_1 c}{k_1 + c}\right).$$  (3)

It is important to note that the pumping efflux measured by [41] was at a steady state $[Ca^{2+}]$. When the $[Ca^{2+}]$ is changing, as it does during oscillations, the rate at which the channel activates and inactivates is important for determining the $[Ca^{2+}]$ flux. Experimental data indicates that activation takes places very quickly, but that inactivation is much slower [15]. It is assumed in the model, as an approximation, that activation is instantaneous. The slow inactivation is modelled by the variable n which satisfies the differential equation

$$\tau_n \frac{dn}{dt} = n_\infty(c) - n$$  (4)

where

$$n_\infty(c) = 1 - \frac{c^2}{k_2^2 + c^2}$$  (5)

and $\tau_n$ is a constant. The rate of inactivation is controlled by the parameter $\tau_n$; the larger the value of $\tau_n$ the slower the rate of inactivation.

The term $\mu(P)$ which appears in the $J_{channel}$ term controls the qualitative behaviour of the system as a function of $[IP_3]$. It determines over what range of $[IP_3]$ values the system without diffusion acts as nonexcitable, excitable, or oscillatory (Section 5.3). It takes the form

$$\mu(P) = \mu_0 + \frac{\mu_1 P}{k_\mu + P}$$  (6)

where $\mu_0$, $\mu_1$, and $k_\mu$ are constants.

The pump term, $J_{pump}$ models the pumping of $Ca^{2+}$ out of the cytosol. It includes pumping out of the cell membrane, as well as back into the ER. It is known that pumping is an increasing function of $[Ca^{2+}]$, and that there is some maximum pumping rate. A simple term that represents this behaviour is

$$J_{pump} = \frac{\gamma c}{k_\gamma + c}$$  (7)

where $k_\gamma$ is a constant.

The term $J_{leak}$ represents a flux due to leakage into the cytosol. It includes leakage through the cell membrane from outside the cell, and leakage from the ER. The leakage flux is caused by diffusion resulting from the separation of two regions at different concentrations . This was taken, for simplicity, as a constant. Therefore

$$J_{leak} = \beta \tag{8}$$

where $\beta$ is a constant.

### 5.2.4 Summary of the Model Equations

The model equations are

$$\frac{\partial P}{\partial t} = D_p(P_{xx} + P_{yy}) - k_p P \tag{9}$$

$$\frac{\partial c}{\partial t} = D_c(c_{xx} + c_{yy}) + J_{channel} - J_{pump} + J_{leak} \tag{10}$$

$$\tau_n \frac{dn}{dt} = n_\infty(c) - n \tag{11}$$

where

$$J_{channel} = k_{flux}\mu(P)n\left(b + \frac{V_1 c}{k_1 + c}\right) \tag{12}$$

$$J_{pump} = \frac{\gamma c}{k_\gamma + c} \tag{13}$$

$$J_{leak} = \beta \tag{14}$$

$$n_\infty(c) = 1 - \frac{c^2}{k_2^2 + c^2} \tag{15}$$

$$\mu(P) = \mu_0 + \frac{\mu_1 P}{k_\mu + P}. \tag{16}$$

The variable P represents $[IP_3]$ and has units of $\mu M$. The variable c represents $[Ca^{2+}]$ and has units of $\mu M$. The variable n represents the fraction of receptors that have not been inactivated by $Ca^{2+}$.

### 5.2.5 Parameter Values

The values of the parameters for the model are given in Table 1. Parameter values were chosen to match up with known experimental results, where these were available.

In many experiments with the Xenopus laevis oocyte in which $[Ca^{2+}]$ waves were observed, the extracellular $[Ca^{2+}]$ was maintained at very low levels [30]. Because of this leakage through the cell membrane was very small. It is assumed that

leakage from the ER is very small as well. Therefore the term $J_{leak}$ was set to zero for all the simulations.

For some experiments on Xenopus laevis oocyte a chemical analogue of $IP_3$ called myoinositol (1,4,5)trisphosphorothioate ($IP_3S_3$) was used [30]. $IP_3S_3$ differs from $IP_3$ in that it does not degrade. Therefore $k_p = 0$ for simulations of this experimental protocol.

Table 1: Parameter values for the model. Parameter values were chosen to match up with known experimental results, where these were available.

| Parameter | Value |
|---|---|
| b | 0.111 |
| $V_1$ | 0.889 |
| $\beta$ | 0.0 |
| $\gamma$ | $2.0\ \mu M \cdot s^{-1}$ |
| $\tau_n$ | 2.0s |
| $k_1$ | $0.7\ \mu M$ |
| $k_2$ | $0.7\ \mu M$ |
| $k_\gamma$ | $0.10\ \mu M$ |
| $k_{flux}$ | $16.0\ \mu M \cdot s^{-1}$ |
| $\mu_0$ | 0.29 |
| $\mu_1$ | 0.30 |
| $k_\mu$ | $4.0\ \mu M$ |
| $k_p$ | $0.0\ s^{-1}$ |
| $J_{leak}$ | $0.0\ \mu M \cdot s^{-1}$ |
| $D_c$ | $20\ \mu m^2 \cdot s^{-1}$ |
| $D_p$ | $300\ \mu m^2 \cdot s^{-1}$ |

## 5.3 The Excitable and Oscillatory Regimes

An insight into the type of solutions the model has may be gained by considering the spatially homogenous equations. That is to say, the equations without diffusion. These equations are ordinary differential equations for which $\mu$ functions as a bifurcation parameter. Plotting the steady state for $[Ca^{2+}]$ versus $\mu$ gives a bifurcation diagram.

The procedure that was followed to find the bifurcation diagram is outlined as follows. Let $[IP_3]$ be a constant, then the equation for $[IP_3]$ may be dropped from the model equations. After dropping the diffusion term in the $[Ca^{2+}]$ equation, and

setting $J_{leak} = 0$, the differential equations for calcium and the inactivation variable n are,

$$\frac{dc}{dt} = k_{flux}\mu(P)n\left(b + \frac{V_1 c}{k_1 + c}\right) - \frac{\gamma c}{k_\gamma + c} \qquad (17)$$

$$\tau_n\frac{dn}{dt} = 1 - \frac{c^2}{k_2^2 + c^2} - n. \qquad (18)$$

These equation contains no spatial dependence, therefore solutions to these equations represent homogeneous behaviour for $[Ca^{2+}]$ and n. All the parameters, except $\mu$, are set by the properties of the receptors and pumps that are involved in the production of calcium waves. The value of $\mu$ ,which is a function of $[IP_3]$, is set by the initial conditions for $[IP_3]$. Therefore varying the initial conditions for $[IP_3]$ is equivalent to varying $\mu$. The bifurcation diagram was found by integrating the equations using the program *Auto*.

The qualitative behaviour of solutions to the spatially homogenous equations depends on the value of $\mu$. For $\mu$ near the first Hopf bifurcation point the behaviour is what is described as excitable. For medium size values of $\mu$ the behaviour is oscillatory. For large $\mu$ the behaviour is nonexcitable. The dependence of the behaviour on the value of $\mu$ may be summarised with a bifurcation diagram (Figure 10).

For $\mu$ just below 0.529 the system exhibits excitable behaviour. A small perturbation away from the steady state is eventually damped out and the system returns to the steady state. However, a perturbation above some threshold will not be damped out but instead will result in a large excursion from the steady state, then an eventual return to the steady state. This is the type of behaviour exhibited by nerve cells, which only fire off an electrical potential when they are simulated above some level.

Between the ranges of 0.529 to 0.814 for $\mu$ the system exhibits oscillatory behaviour. The steady state is unstable and any perturbation away from the steady state results in oscillations. Unlike excitable systems there is no threshold that has to be passed for a large excursion away from the steady state to occur. The transition from excitable to oscillatory behaviour occurs via a supercritical Hopf bifurcation at $\mu = 0.529$.

If $\mu$ is much less than 0.529, or greater than 0.814 the system is nonexcitable. A small perturbation away from the steady state is damped out and the system returns to the steady state. No excitable or oscillatory behaviour is exhibited.
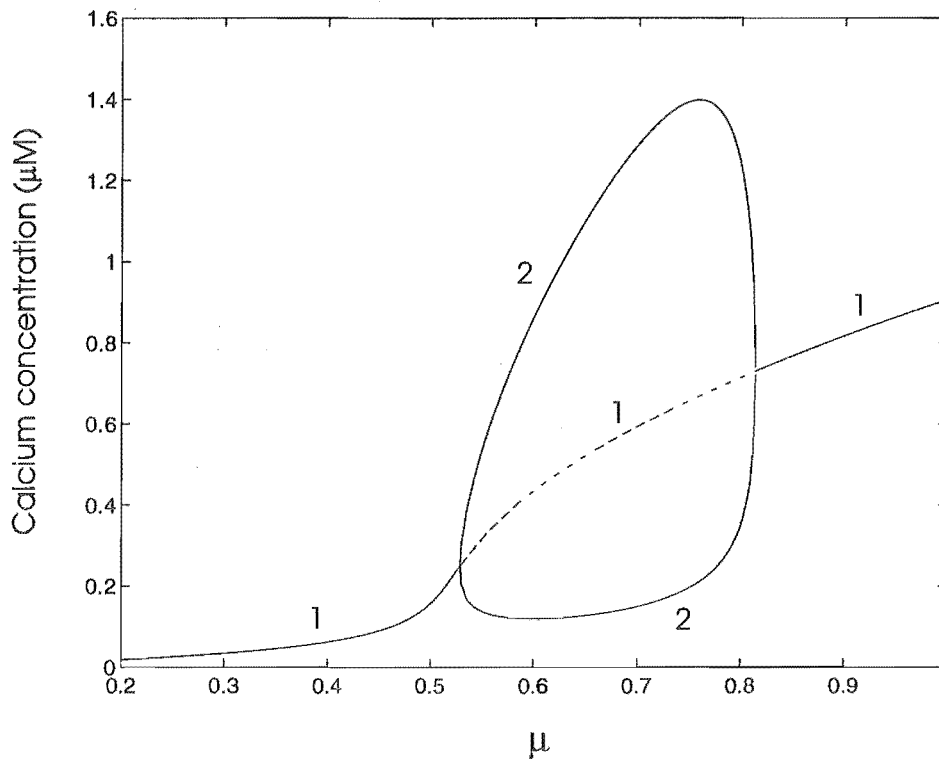
Figure 10: Bifurcation diagram for the spatially homogenous model equations at constant P ($[IP_3]$). A supercritical Hopf bifurcation occurs at $\mu = 0.529$ and a supercritical Hopf bifurcation occurs at $\mu = 0.814$. For $\mu$ slightly less than 0.529 the system exhibits excitable behaviour. For $0.529 < \mu < 0.814$ the behaviour of the system is oscillatory. When $\mu$ is much less than 0.529, or greater than 0.814, the behaviour is nonexcitable. Curve 1 is the steady state for the system. The dashed line represents an unstable steady state. Curve 2 is the minimum and maximum values for oscillations when the behaviour is oscillatory. The parameter values for the model equations are as shown in Table 3. Note that these parameters are slightly different from those in Table 1. For the parameters shown in Table 1 the bifurcation diagram is similar except that the oscillatory regime is $0.29 < \mu < 0.50$. However, because of the steepness of the curve near $\mu = 0.29$, *Auto* was unable to find the amplitude of the oscillations in the oscillatory regime.

# 6 Computational Methods

## 6.1 Introduction

The equation for P ($[IP_3]$) is a diffusion equation and was solved using the Peaceman-Rachford algorithm, an alternating direction implicit (ADI) method. The equation for c ($[Ca^{2+}]$) is a reaction-diffusion equation and was solved using a generalisation of the Peaceman-Rachford algorithm. The ordinary differential equation for n (the inactivation variable) was solved using a second order Taylor series approximation.

## 6.2 Alternating Direction Implicit (ADI) Method

### 6.2.1 Introduction

ADI is a finite difference method that is particularly useful for solving parabolic partial differential equations. The method reduces a two dimensional problem to a sequence of one dimensional problems, one in the x direction and the other in the y direction. The one dimensional problems involve the solution of a tridiagonal system of linear equations, for which very efficient algorithms are available.

The two dimensional diffusion equation may be solved using an ADI method called the Peaceman-Rachford algorithm [43]. The equation for P ($[IP_3]$) with $k_p = 0$ is a two dimensional diffusion equation so may be solved using this algorithm. This is not the case for the c ($[Ca^{2+}]$) equation which includes a reaction term as well. However the Peaceman-Rachford algorithm may be generalised slightly so that it may be used for solving two dimensional reaction-diffusion equations as well.

### 6.2.2 ADI for the Diffusion Equation

The diffusion equation in two dimensions is

$$u_t = D(u_{xx} + u_{yy}). \tag{19}$$

In [52] various ADI schemes for solving this problem are derived. In particular an algorithm called the Peaceman-Rachford algorithm is derived. The derivation given by Strikwerda is outlined in what follows. The derivation is modified slightly for explanatory reasons.

Let $h$ be an increment in the x or y direction, and $k$ be an increment in time. Then a second order Taylor series approximation to $Du_{xx}$ can be written as a weighted average of the central difference approximations at time $t$, and time $t + k$

$$
\begin{aligned}
Du_{xx}(x,y,t) &= \frac{D}{2h^2}[u(x+h,y,t+k) - 2u(x,y,t+k) + u(x-h,y,t+k)] \\
&+ \frac{D}{2h^2}[u(x+h,y,t) - 2u(x,y,t) + u(x-h,y,t)] + O(h^2). \tag{20}
\end{aligned}
$$

Likewise for $Du_{yy}$

$$
\begin{aligned}
Du_{yy}(x, y, t) &= \frac{D}{2h^2}[u(x, y+h, t+k) - 2u(x, y, t+k) + u(x, y-h, t+k)] \\
&+ \frac{D}{2h^2}[u(x, y+h, t) - 2u(x, y, t) + u(x, y-h, t)] + O(h^2). \quad (21)
\end{aligned}
$$

Let $A_1$ be an operator standing for the central difference approximation in the x-direction, and $A_2$ be an operator standing for the central difference approximation in the y-direction. In addition let n stand for the value of u at time $t$, and $n+1$ stand for the value of u at time $t+k$. Then using this more compact notation the approximations (20) and (21) may be written as

$$
Du_{xx}(x, y, t) = \frac{1}{2}(A_1 u^{n+1} + A_1 u^n) + O(h^2) \quad (22)
$$

$$
Du_{yy}(x, y, t) = \frac{1}{2}(A_2 u^{n+1} + A_2 u^n) + O(h^2). \quad (23)
$$

A second order Taylor series approximation for $u_t$ is:

$$
u_t = \frac{1}{k}[u(x, t+k) - u(x, t)] + O(k^2). \quad (24)
$$

Substituting the approximations (22), (23), and (24) into the diffusion equation (19) gives the discrete equation

$$
\frac{u^{n+1} - u^n}{k} = \frac{1}{2}(A_1 u^{n+1} + A_1 u^n) + \frac{1}{2}(A_2 u^{n+1} + A_2 u^n) + O(k^2) + O(h^2). \quad (25)
$$

Rearranging this gives

$$
\begin{aligned}
(1 - \frac{k}{2}A_1 - \frac{k}{2}A_2)u^{n+1} &= (1 + \frac{k}{2}A_1 + \frac{k}{2}A_2)u^n \quad (26) \\
&+ O(k^3) + O(kh^2) \quad (27)
\end{aligned}
$$

Adding $(k^2 A_1 A_2 u^{n+1})/4$ to both sides, and using the formula

$$
(1 \pm a_1)(1 \pm a_2) = 1 \pm a_1 \pm a_2 + a_1 a_2 \quad (28)
$$

results in

$$
\begin{aligned}
(I - \frac{k}{2}A_1)(1 - \frac{k}{2}A_2)u^{n+1} &= (I + \frac{k}{2}A_1)(I + \frac{k}{2}A_2)u^n \\
&+ \frac{k^2}{4}A_1 A_2(u^{n+1} - u^n) \\
&+ O(k^3) + O(kh^2) \quad (29)
\end{aligned}
$$

The second term on the right-hand side is $O(k^3)$ so may be incorporated into the $O(k^3)$ term. Dropping the $O(k^3)$ and $O(kh^2)$ terms, and letting U start for the dependent variable in the equations then (29) becomes

$$(I - \frac{k}{2}A_1)(I - \frac{k}{2}A_2)U^{n+1} = (I + \frac{k}{2}A_1)(I + \frac{k}{2}A_2)U^n \tag{30}$$

The Peaceman-Rachford algorithm solves this equation using the two phase process

$$(I - \frac{k}{2}A_1)\tilde{U}^{n+\frac{1}{2}} = (I + \frac{k}{2}A_2)U^n \tag{31}$$

$$(I - \frac{k}{2}A_2)U^{n+1} = (I + \frac{k}{2}A_1)\tilde{U}^{n+\frac{1}{2}}. \tag{32}$$

Expanding out the operator terms, substituting $\alpha = (Dk)/h^2$, and rearranging terms gives the computational form (Figure 11)

$$-\alpha U_{j-1,l}^{n+\frac{1}{2}} + 2(1+\alpha)U_{j,l}^{n+\frac{1}{2}} - \alpha U_{j+1,l}^{n+\frac{1}{2}} = \alpha U_{j,l-1}^n + 2(1-\alpha)U_{j,l}^n + \alpha U_{j,l+1}^n \tag{33}$$

$$-\alpha U_{j,l-1}^{n+1} + 2(1+\alpha)U_{j,l}^{n+1} - \alpha U_{j,l+1}^{n+1} = \alpha U_{j-1,l}^{n+\frac{1}{2}} + 2(1-\alpha)U_{j,l}^{n+\frac{1}{2}} + \alpha U_{j+1,l}^{n+\frac{1}{2}}. \tag{34}$$
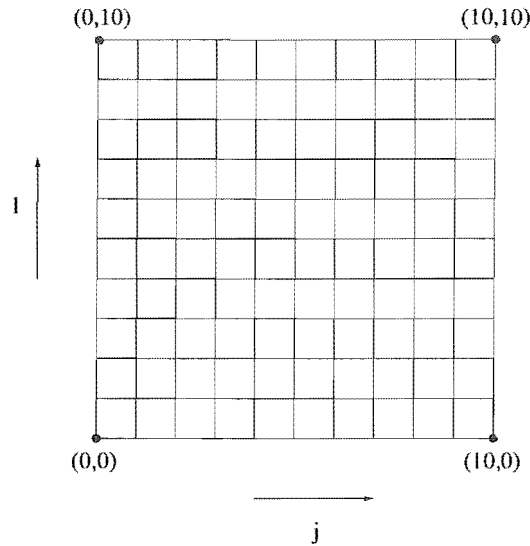


Figure 11: Grid structure for ADI. The x-direction is denoted by j and the y-direction by l. The increment in the x and y directions is h.

There are two phases to the Peaceman-Rachford algorithm. The first phase uses equation (33) and is in the x-direction. This equation represents a tridiagonal system of linear equations in the dependent variables $U^{n+\frac{1}{2}}$. It is important to note that the $U^{n+\frac{1}{2}}$ values are not accurate representations of U at time $n+\frac{1}{2}$, but are best thought of as intermediate values in the two phase algorithm. Once the $U^{n+\frac{1}{2}}$ values are found they are substituted into the right-hand side of equation (34). Solving (34) for the values $U^{n+1}$ completes phase 2 of the algorithm.

### 6.2.3 ADI for the Reaction-Diffusion Equation

The reaction-diffusion equation includes a reaction term $f(u, x, y, t)$ and is of the form

$$u_{tt} = D(u_{xx} + u_{yy}) + f(u, x, y, t). \tag{35}$$

As before the second order approximations (22),(23), and (24) are used for $Du_{xx}$, $Du_{yy}$, and $u_t$. Substituting these in then dropping $O(k^3)$ and $O(kh^2)$ terms gives

$$(I - \frac{k}{2}A_1)(I - \frac{k}{2}A_2)U^{n+1} = (I + \frac{k}{2}A_1)(I + \frac{k}{2}A_2)U^n + kf(U^n). \tag{36}$$

This equation is the reaction-diffusion equivalent of (30). The similarity suggests that a plausible scheme for solving (36) is the two phase scheme

$$(I - \frac{k}{2}A_1)\tilde{U}^{n+\frac{1}{2}} = (I + \frac{k}{2}A_2)U^n + akf(U^n) \tag{37}$$

$$(I - \frac{k}{2}A_2)U^{n+1} = (I + \frac{k}{2}A_1)\tilde{U}^{n+\frac{1}{2}} + bkf(U^n) \tag{38}$$

where a and b are constants.
Multiplying (38) by $(I - \frac{k}{2}A_1)$, and substituting for $(I - \frac{k}{2}A_1)\tilde{U}^{n+\frac{1}{2}}$ using (37) results in

$$
\begin{aligned}
(I - \frac{k}{2}A_1)(I - \frac{k}{2}A_2)U^{n+1} = {} & (I + \frac{k}{2}A_1)(I + \frac{k}{2}A_2)U^n + \\
& \{a(I + \frac{k}{2}A_1) + b(I - \frac{k}{2}A_1)\} + kf(U^n).
\end{aligned}
$$

For this to be consistent with (36) then

$$a(I + \frac{k}{2}A_1) + b(I - \frac{k}{2}A_1) = I.$$

This can only be satisfied if

$$a = \frac{1}{2} \quad , \quad b = \frac{1}{2}. \tag{39}$$

Therefore a generalisation of the Peaceman-Rachford algorithm appropriate for the reaction-diffusion equation is

$$(I - \frac{k}{2}A_1)\tilde{U}^{n+\frac{1}{2}} = (I + \frac{k}{2}A_2)U^n + \frac{1}{2}kf(U^n) \tag{40}$$

$$(I - \frac{k}{2}A_2)U^{n+1} = (I + \frac{k}{2}A_1)\tilde{U}^{n+\frac{1}{2}} + \frac{1}{2}kf(U^n). \tag{41}$$

Expanding out the operator terms, substituting $\alpha = (Dk)/h^2$, and rearranging terms gives the computational form

$$-\alpha U_{j-1,l}^{n+\frac{1}{2}} + 2(1+\alpha)U_{j,l}^{n+\frac{1}{2}} - \alpha U_{j+1,l}^{n+\frac{1}{2}} = \alpha U_{j,l-1}^n + 2(1-\alpha)U_{j,l}^n + \alpha U_{j,l+1}^n + kf(U_{j,l}^n) \tag{42}$$

$$-\alpha U_{j,l-1}^{n+1} + 2(1+\alpha)U_{j,l}^{n+1} - \alpha U_{j,l+1}^{n+1} = \alpha U_{j-1,l}^{n+\frac{1}{2}} + 2(1-\alpha)U_{j,l}^{n+\frac{1}{2}} + \alpha U_{j+1,l}^{n+\frac{1}{2}} + kf(U_{j,l}^n) \tag{43}$$

## 6.3 Taylor Series Solution for the Inactivation Variable

The inactivation variable equation is

$$\frac{dn}{dt} = \frac{1}{\tau_n}\left\{1 - \frac{c^2}{k_2 + c^2} - n\right\}. \tag{44}$$

Let

$$K = \frac{1}{\tau_n}\left\{1 - \frac{c^2}{k_2^2 + c^2}\right\} \tag{45}$$

then

$$\frac{dn}{dt} = K - \frac{1}{\tau_n}n \tag{46}$$

A Taylors series expansion for n is

$$n(t_0 + \Delta t) = n_0 + \left\{K - \frac{n_0}{\tau_n}\right\}\left\{\Delta t - \frac{(\Delta t)^2}{2\tau_n}\right\} \tag{47}$$

Substituting back for K gives the update formula for a time step of $\Delta t$ as

$$n^{k+1} = n^k + \frac{1}{\tau_n}\left\{1 - \frac{c^2}{k_2^2 + c^2} - n^k\right\}\left\{\Delta t - \frac{(\Delta t)^2}{2\tau_n}\right\} \tag{48}$$

Table 2: NAG subroutines used

| NAG subroutine | Function of subroutine |
|---|---|
| c05adf | Root finder |
| f01lef | Pre-factorisation scheme for f04lef |
| f04lef | Tridiagonal system solver |
| f01brf | Pre-factorisation scheme for f04axf |
| f04axf | Sparse linear system solver |

## 6.4 Implementation of Numerical Methods

The numerical algorithms were coded in the computer language Fortran. Use was made of NAG library subroutines for certain parts of the code (Table 2)

Most simulations were run on a 240 by 240 square grid, with a time step of 0.05 seconds used for all simulations. Some simulations were run on a smaller grid size in order to check the effect of the grid size on the stability of spirals . At each time step $[IP_3]$, $[Ca^{2+}]$ and n were solved for on the grid. The $[Ca^{2+}]$ values were output at each time step using the Spyglass library routine d8pimg, which converts an array into an HDF file.

These file were viewed using the Spyglass program Transform. Transform is a program specifically designed for viewing two-dimensional data. Data can be viewed either in contour form, or as a colour-coded image using a wide variety of colour codings. A particularly useful feature of Transform is its ability to form animations from a sequence of images. This makes it easy to discern patterns in the data. The animation feature was used to observe the formation of $[Ca^{2+}]$ spirals and their breakup.

A variety of checks were made to ensure that the numerical method worked. A simple diffusion problem, for which an analytical solution was available, was solved using the numerical method. The analytical and numerical solutions were then compared and found to agree. Some simulations were run which emulated previous simulations of the full partial differential equation system. The previous simulations had used a different numerical method, but the solutions were found to agree with the ADI numerical method. As an additional check the same system was solved for a variety of problems using the method of lines (MOL) [45],[48]. These solutions also agreed with the ADI method solutions. The ADI method was used instead of the MOL because it was an order of magnitude faster.

# 7 The Formation of a Stable Spiral

## 7.1 Introduction

There exist a variety of ways of initiating spiral waves [17]. However, experimentally, some of these methods are less plausible than others. The method that was used here to initiate a stable spiral closely follows what can be done experimentally. Basically blocks of $IP_3$ were used to generate travelling $[Ca^{2+}]$ waves. These were blocked by regions of low $[Ca^{2+}]$ leading to the bending of the waves, and eventually the formation of spiral waves. For simplicity the simulations were done on a square grid, and no flux boundary conditions were used.

## 7.2 No Flux Boundary Conditions

For simplicity the simulations were made on a square grid. The grid was indexed by j in the x-direction and l in the y-direction (Figure 12).
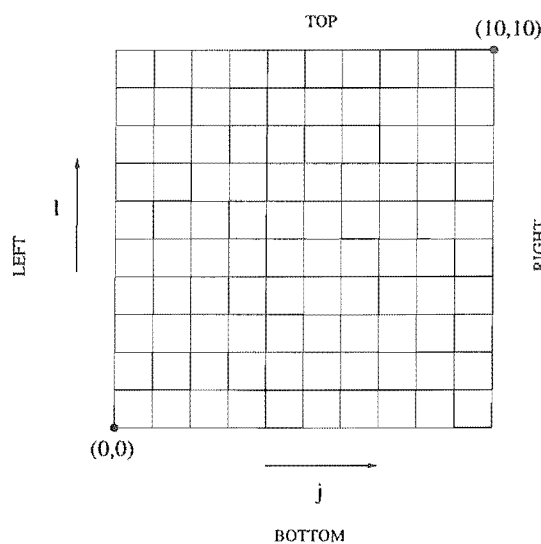


Figure 12: No flux boundary conditions on a 10 by 10 grid. The square grid is indexed by j in the x-direction and l in the y-direction. In the actual simulations the grid size was 240 by 240.

No flux boundary conditions were set for P ($[IP_3]$) and c ($[Ca^{2+}]$) at the boundaries. This simulates the no flux boundary conditions in the experiments. In mathematical terms no flux boundary conditions are equivalent to

$$\frac{\partial U}{\partial x} = 0 \qquad \text{on the left and right side boundaries and,} \qquad (49)$$

$$\frac{\partial U}{\partial y} = 0 \qquad \text{on the top and bottom boundaries.} \qquad (50)$$

where U stands for either P or c.

For phase 1 of ADI the computational formula is

$$-\alpha U_{j-1,l}^{n+\frac{1}{2}} + 2(1+\alpha)U_{j,l}^{n+\frac{1}{2}} - \alpha U_{j+1,l}^{n+\frac{1}{2}} = \alpha U_{j,l-1}^{n} + 2(1-\alpha)U_{j,l}^{n} + \alpha U_{j,l+1}^{n} + kf(U_{j,l}). \quad (51)$$

If the computational formula is applied at the left side boundary $(j = 0)$ then

$$-\alpha U_{-1,l}^{n+\frac{1}{2}} + 2(1+\alpha)U_{0,l}^{n+\frac{1}{2}} - \alpha U_{1,l}^{n+\frac{1}{2}} = \alpha U_{0,l-1}^{n} + 2(1-\alpha)U_{0,l}^{n} + \alpha U_{0,l+1}^{n} + kf(U_{0,l}) \quad (52)$$

This introduces a fictitious point $U_{-1,l}^{n+\frac{1}{2}}$ into the left hand side of the equation. However, on the left side boundary the no flux boundary condition (49) applies. A central difference approximation to this boundary condition is

$$\frac{U_{1,l} - U_{-1,l}}{2h} = 0 \qquad (53)$$

$$\Rightarrow U_{-1,l} = U_{1,l}. \qquad (54)$$

Thus the fictitious point in (52) may be eliminated, and the finite difference formula for the left side boundary becomes

$$2(1+\alpha)U_{0,l}^{n+\frac{1}{2}} - 2\alpha U_{1,l}^{n+\frac{1}{2}} = \alpha U_{0,l-1}^{n} + 2(1-\alpha)U_{0,l}^{n} + \alpha U_{0,l+1}^{n} + kf(U_{0,l}). \qquad (55)$$

Fictitious points also occur when the computational formula is applied to the right side boundary, and are eliminated in a similar manner. Likewise for phase 2 of the ADI method. The resulting equations for phase 1 and phase 2 are tridiagonal. Very efficient algorithms exist for the solution of tridiagonal systems.

## 7.3  Initial Conditions for the Generation of a Stable Spiral

At time $t = 0$ $[IP_3]$ is set to zero over the grid. $[Ca^{2+}]$ and n are set at the steady state values for $[IP_3]$ equal to zero. If the system is left with these initial conditions then $[IP_3]$ will stay at zero, and $[Ca^{2+}]$ and n will stay at their steady state values. However if a perturbation is applied to the system just after the time $t = 0$ then the

steady state will be disrupted. In particular if blocks of $[IP_3]$ and $[Ca^{2+}]$ are applied in the right places,for the right length of time, then a single stable spiral will form.

The particular configuration of $[IP_3]$ and $[Ca^{2+}]$ that was used to generate a stable spiral is shown in Figure 13. As may be done experimentally, blocks of $IP_3$ are released after time $t = 0$ . These blocks trigger the release of travelling wave of $[Ca^{2+}]$ . Blocks of low $[Ca^{2+}]$ , representing temporary inhomogeneities in the cytoplasm, block the passage of these waves causing them to bend. Eventually spiral waves form.
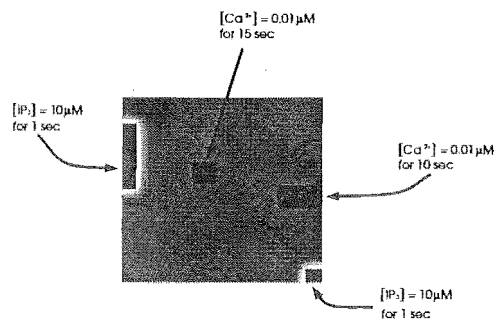


Figure 13: Initial conditions for a stable spiral. At time $t = 0$ $[IP_3]$ is set to zero, and $[Ca^{2+}]$ and n are set to the corresponding steady states. After time $t = 0$ blocks of $[IP_3]$ and $[Ca^{2+}]$ are set for certain lengths of time. When the blocks are released $IP_3$ and $Ca^{2+}$ are allowed to diffuse through the square.

## 7.4 Results

Within about 50 seconds a spiral began to form near one of regions that had a initial low $[Ca^{2+}]$ . This spiral continued to grow in size until the spiral arms filled the entire square in which the simulation took place. During this time the centre of the spiral wave remained unchanged. The resulting spiral was stable up to at least t $= 3000$ seconds (Figure 14).

(a)  † = 0.75s

(b)  † = 5.0s

(c)  † = 55.5s

(d)  † = 124.2s

(e)  † = 259.0s

(f)  † = 462.7s
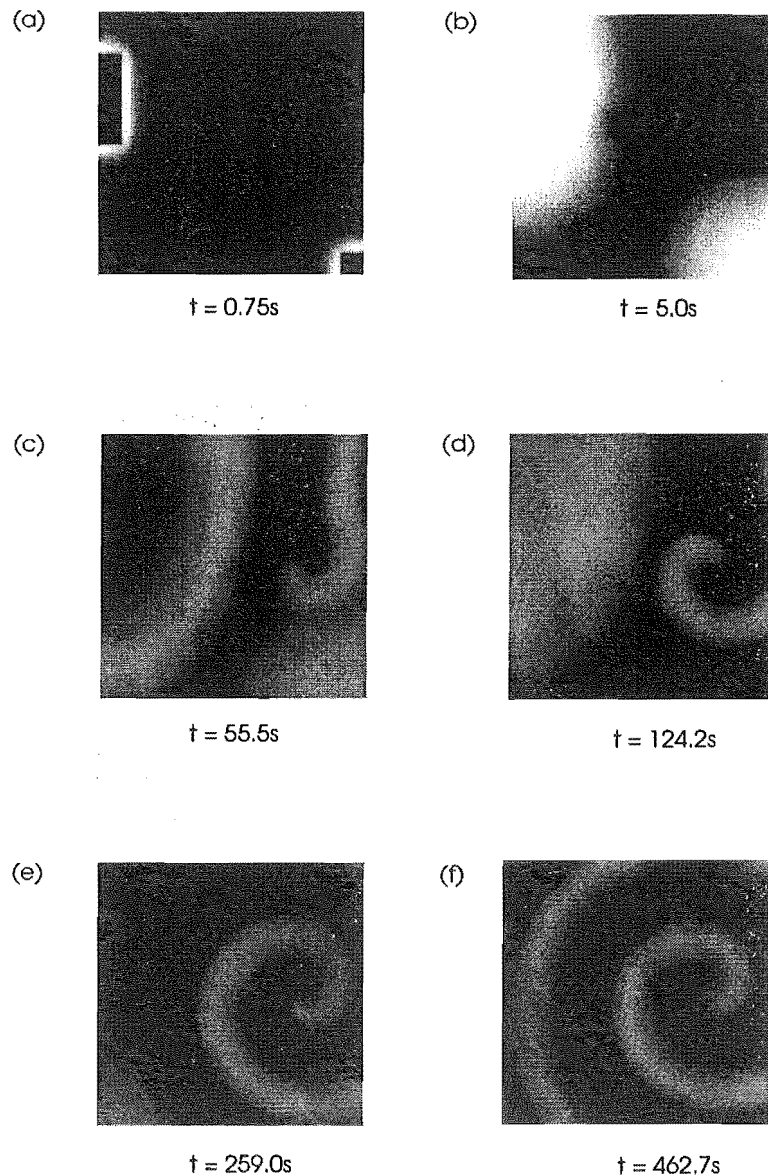
Figure 14: Formation of a stable spiral. Cell size $= 250 \ \mu m$ by $250 \ \mu m$, grid size $= 240$ by $240$. The boundary conditions are no flux. The parameter values for the simulation are given in Table 1. The light areas represent regions of high $[Ca^{2+}]$, the dark areas regions of low $[Ca^{2+}]$. (a) Initial conditions. The black rectangles are regions with a low $[Ca^{2+}]$. The white outlined rectangles mark the two areas with an above steady state $[IP_3]$. See Figure 13 for more details on the initial conditions. (b) The regions with an initial above steady state $[IP_3]$ initiate travelling $[Ca^{2+}]$ waves. (c) A spiral begins to form near one of the regions where a low $[Ca^{2+}]$ was set up as part of the initial conditions (d) This spiral grows in size. (e) The $[Ca^{2+}]$ travelling wave patterns die away, and the spiral develops further. (f) The spiral forms another loop. This pattern is stable up to at least $t = 3000$ seconds.

## 7.5 Discussion

With the right choice of parameter values , and for certain initial conditions , a stable spiral forms in the model equations .This spiral is stable for at least 3000 seconds. Stable spirals are also observed in experiments with the Xenopus laevis oocyte. These are commonly initiated by the bending of $[Ca^{2+}]$ waves by refractory regions of $[Ca^{2+}]$ . This same mechanism in the model simulations also produces spiral waves, and the simulation results suggest one set of initial conditions for which a stable spiral will form.

It has been suggested that an excitable medium has a unique spiral solution [60]. In this proposal the parameters of the model set the wavelength and period of the spiral, and the initial conditions set the phase and location of the spiral. For this particular simulation the long term $[IP_3]$ is $0.634\mu M$ and the corresponding $\mu$ value is 0.331 . This places the system in the oscillatory regime for the system $(0.29 < \mu < 0.50)$, as opposed to the excitable regime. An unanswered question is whether or not there is a unique stable spiral solution for an oscillatory system? That is to say, do all the spirals that form have the same wavelength and period? A more detailed set of simulations, with a wide variety of initial conditions, could go some way towards answering this question.

As yet, a comprehensive analysis of the period and wavelength of spirals that occur in experiments with Xenopus laevis has still to made. A comparison between the experimental and simulation results would allow further refinements to be made to the model. If there is a unique stable spiral solution in the oscillatory regime then this would tightly constrain the parameter values that the model can take.

# 8 The Formation of Unstable Spirals

## 8.1 Introduction

It is apparent from the previous section that with certain initial conditions and parameter values a stable spiral will form in the model equations. For the stable spiral simulation the long term $[IP_3]$ is $0.634\mu M$ and the corresponding $\mu$ value is $0.331$. This places the system in the oscillatory regime for the system ($0.29 < \mu < 0.50$). An important question is whether or not there is a unique spiral solution for an oscillatory system, or do a number of different stable spiral wave solutions exist?

In the stable spiral simulation blocks of $IP_3$ were used to generate $[Ca^{2+}]$ travelling waves. These were then bent by regions that were at a low $[Ca^{2+}]$ to form spiral waves. This suggests that if periodic $[Ca^{2+}]$ waves are set up as initial conditions, then broken by a region of low $[Ca^{2+}]$ , then spirals will form. Moreover periodic $[Ca^{2+}]$ waves with different wavelengths and periods may form spirals with different arm widths and rotation periods.

Periodic $[Ca^{2+}]$ wave solutions were found to the model equations by transforming to travelling wave coordinates, then finding the limit cycle solution to the resulting system of ordinary differential equations. With no flux boundary conditions a periodic wave flattens and the wavelength increases. This flattening effect may influence the stability properties of the spiral that form. To guard against this periodic boundary conditions were used for $[Ca^{2+}]$ and $[IP_3]$.

The parameter values as shown in Table 3 were used. These are a slightly more up to date set of parameters then the set used in the previous simulation. However, while they are slightly different, this is expected to have little qualitative effect on the type of solutions obtained.

## 8.2 Periodic Wave Solutions

### 8.2.1 Introduction

Periodic one dimensional wave solutions were found to the model equations by transforming to travelling wave coordinates, then finding the limit cycle solution to the resulting system of ordinary differential equations. The two free parameters in the system of ordinary differential equations were P ($[IP_3]$) and v (the wave speed). P was set at a value of 1.5 $\mu M$, a high enough value to ensure the system was operating in the oscillatory regime. The wave speed v was set a number of different values, these corresponding to periodic waves of different wavelengths and periods.

Table 3: Parameter values for the model. Parameter values were chosen to match up with known experimental results, where these were available.

| Parameter | Value |
|-----------|-------|
| b | 0.111 |
| $V_1$ | 0.889 |
| $\beta$ | 0.0 |
| $\gamma$ | $2.2\ \mu M \cdot s^{-1}$ |
| $\tau_n$ | 2.0s |
| $k_1$ | $0.7\ \mu M$ |
| $k_2$ | $0.7\ \mu M$ |
| $k_\gamma$ | $0.17\ \mu M$ |
| $k_{flux}$ | $8.1\ \mu M \cdot s^{-1}$ |
| $\mu_0$ | 0.0 |
| $\mu_1$ | 1.0 |
| $k_\mu$ | $0.7\ \mu M$ |
| $k_p$ | $0.0\ s^{-1}$ |
| $J_{leak}$ | $0.0\ \mu M \cdot s^{-1}$ |
| $D_c$ | $25\ \mu m^2 \cdot s^{-1}$ |
| $D_p$ | $300\ \mu m^2 \cdot s^{-1}$ |

## 8.2.2 Travelling Wave Coordinates

Transforming to travelling wave coordinates $z = x - vt$ , where $v$ is the speed of the travelling wave, gives the system of ordinary differential equations

$$D_c \frac{dg}{dz} = -vg - k_{flux} n \left( \frac{P}{0.7 + P} \right) \left( b + \frac{V_1 c}{k_1 + c} \right) + \frac{\gamma c}{k_\gamma + c} \tag{56}$$

$$\frac{dc}{dz} = g \tag{57}$$

$$\frac{1}{\tau_v} \frac{dn}{dz} = n - \frac{k_2^2}{k_2^2 + c^2} \tag{58}$$

where the substitution $g = \frac{dc}{dz}$ has been made. For a certain range of values for P and v this system this system of ordinary differential equations possesses limit cycle solutions. The limit cycle solutions correspond to periodic wave solutions to the model equations.

The two parameters that are not set in the travelling wave equations are P ($[IP_3]$) and v the wave speed. Setting a value for P determines the background constant $[IP_3]$, and setting v determines the speed of the travelling wave solution. Not all values of P and v admit travelling wave solutions (Figure 15).
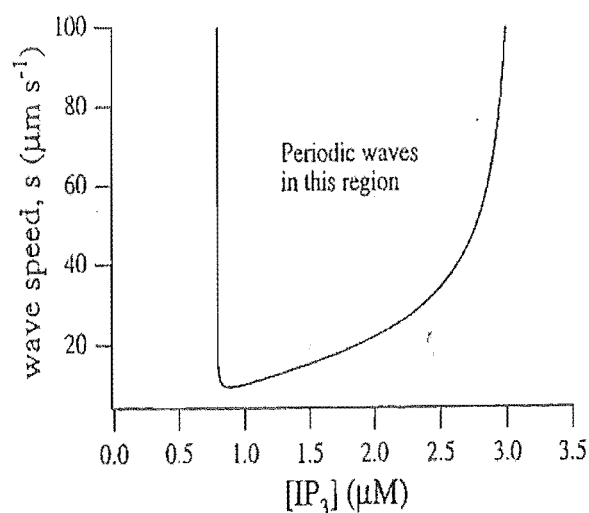


Figure 15: Periodic wave solutions only occur for certain values of P ($IP_3$), and the wave speed (v).

### 8.2.3 Limit Cycle Solutions

P and v were set to values for which periodic waves solutions exist. All simulations were run with P set at a constant value of $1.5\mu M$. This corresponds to a $\mu$ value of 0.68 . For a given value of P there are many possible values of v for which periodic wave solution exist (Figure 15). Setting v selects a periodic wave moving at the constant speed v.

The system of equations were solved using $ode15s$, a Matlab routine for solving stiff systems of ordinary differential equations [46]. Due to the nature of the differential equations it was not possible to find the limit cycle by simply integrating forward or backward in time. Instead the limit cycle had to found by trial and error. The initial conditions for g and c were set at $7.8717 \times 10^{-5} \mu m \cdot s^{-1}$ and 0.59645 $\mu M$ respectively. The particular initial conditions chosen for g and n are not that important. The initial condition for n was varied until it lay on the limit cycle curve. For example, for $v = 40\mu m \cdot s^{-1}$ an n value of 0.436885 is on the limit cycle (Figure 16). The corresponding travelling wave solutions are shown in Figure 17 .
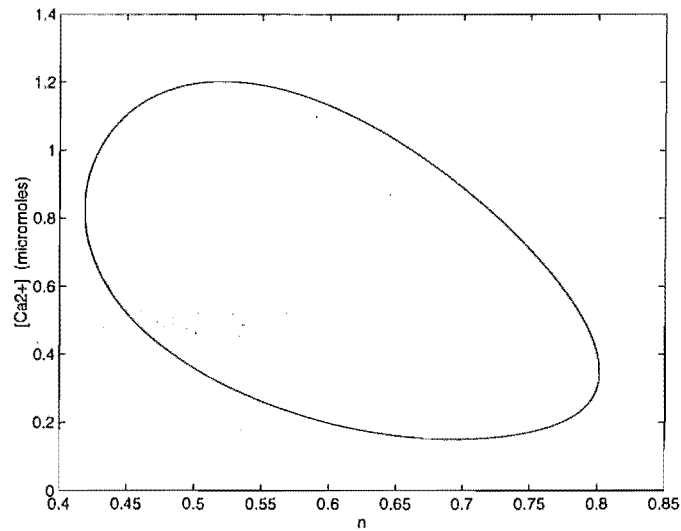
Figure 16: Limit cycle solution in the c-n plane. The initial conditions were $g = 7.8717 \times 10^{-5} \mu m \cdot s^{-1}$, $c = 0.59645 \ \mu M$, and $n = 0.436885$. P was set at $1.5 \mu M$ and v at $40 \ \mu m \cdot s^{-1}$.
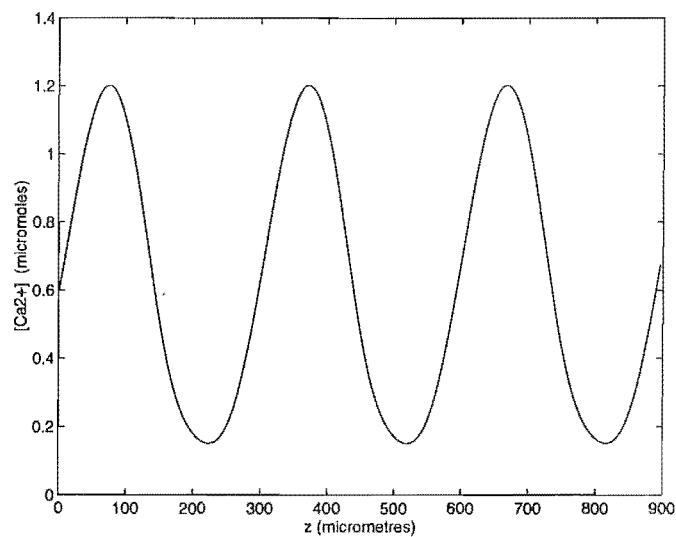


Figure 17: Travelling wave solutions. The initial conditions were $g = 7.8717 \times 10^{-5} \mu m \cdot s^{-1}$, $c = 0.59645 \ \mu M$, and $n = 0.436885$. P was set at $1.5 \mu M$ and v at $40 \ \mu m \cdot s^{-1}$.

## 8.3 Periodic Boundary Conditions

### 8.3.1 Introduction

Periodic boundary conditions were applied on the top and bottom sides, the periodic waves travelling from the bottom to the top. The left and right side boundary conditions were no flux. Without periodic boundary conditions on the top and bottom sides an initial periodic wave will not retain its shape, and eventually the values at the boundaries will not match. However periodic boundary conditions change the structure of the matrix equations for the ADI method. They are no longer tridiagonal, but are sparse, so have to be solved by a different algorithm.

### 8.3.2 Periodic Boundary Conditions for the ADI Method

Introducing fictitious points around the outside of the boundary, then periodic boundary conditions on the bottom and top require that

$$U_{j,1} = U_{j,ng+1} \tag{59}$$

$$U_{j,-1} = U_{j,ng-1} \tag{60}$$

Subtracting (60) from (59) results in

$$U_{j,1} - U_{j,-1} = U_{j,ng+1} - U_{j,ng-1} \tag{61}$$

This condition is equivalent to the requirement that the first derivative matches at the top and bottom side boundaries. To see this, note that the central difference approximation to the first derivative at the bottom and top boundaries are

$$\text{at x} = 0 \quad \frac{\partial U}{\partial x} \approx \frac{U_{j,1} - U_{j,-1}}{2h} \tag{62}$$

$$\text{at x} = L \quad \frac{\partial U}{\partial x} \approx \frac{U_{j,ng+1} - U_{j,ng-1}}{2h} \tag{63}$$

Equating (62) and (63) gives (61).

Phase 1 of the ADI method sweeps in the x-direction. Periodic boundary conditions on the bottom and top do not change the tridiagonal structure of the matrix, though the right hand side is different. However for phase 2 which sweeps in the y-direction the tridiagonal structure is not retained.

For phase 2 of ADI the finite difference formula for the interior points is

$$-\alpha U_{j,l-1}^{n+1} + 2(1+\alpha)U_{j,l}^{n+1} - \alpha U_{j,l+1}^{n+1} = \alpha U_{j-1,l}^{n+\frac{1}{2}} + 2(1-\alpha)U_{j,l}^{n+\frac{1}{2}} + \alpha U_{j+1,l}^{n+\frac{1}{2}} \tag{64}$$

Applying this at the bottom side (l = 0), and using (60) gives the finite difference formula

$$2(1+\alpha)U_{j,0}^{n+1} - \alpha U_{j,1}^{n+1} - \alpha U_{j,ng-1}^{n+1} = \alpha U_{j-1,0}^{n+\frac{1}{2}} + 2(1-\alpha)U_{j,0}^{n+\frac{1}{2}} + \alpha U_{j+1,0}^{n+\frac{1}{2}} \qquad (65)$$

These equations do not have a tridiagonal matrix structure. Instead their structure has the block form

$$\begin{bmatrix} A & & & & & \\ & A & & & & \\ & & A & & & \\ & & & \ddots & & \\ & & & & A & \\ & & & & & A \end{bmatrix}$$

where A is the matrix

$$\begin{bmatrix} 2(1+\alpha) & -\alpha & 0 & 0 & \cdots & 0 & 0 & -\alpha \\ -\alpha & 2(1+\alpha) & -\alpha & 0 & \cdots & 0 & 0 & 0 \\ 0 & -\alpha & 2(1+\alpha) & -\alpha & \cdots & 0 & 0 & 0 \\ \vdots & & & & & & & \vdots \\ 0 & 0 & 0 & 0 & \cdots & -\alpha & 2(1+\alpha) & -\alpha \\ -\alpha & 0 & 0 & 0 & \cdots & 0 & -\alpha & 2(1+\alpha) \end{bmatrix}$$

The $-\alpha$ term in the corner of this matrix breaks the tridiagonal structure. These matrix equations, with an appropriate right hand side, form a sparse system. An algorithm specifically designed for sparse systems was used to solve these matrix equations (see Section 6.4).

## 8.4 Initial Conditions On a Square Grid

Initial conditions for $[Ca^{2+}]$ and n were for a periodic travelling wave, as was found from solving the limit cycle equations. The square size was set so that a whole number of wavelengths would fit within the square from the bottom side to the top side. The boundary conditions on the top and bottom were periodic, and no flux on the left and right hand sides. A wave set up in this way will keep propagating, leaving the top and reappearing at the bottom.

A square block of low $[Ca^{2+}]$ was used to perturb the system (Figure 18). The square block always had the same relative size and position in the square. The $[Ca^{2+}]$ in the block was set at 0.02 $\mu M$, and held at this level for 10 seconds. When

the block is released a spiral wave begins to form at the centre of the square grid. Simulations were run with the wave speed at a number of different values, these values corresponding to different wavelengths and periods for the waves (Table 4).

Table 4: Periodic wave initial conditions. Periodic wave solutions were found by transforming the model equations into travelling wave coordinates, then finding the limit cycle solution to the resulting system of ordinary differential equations.

| Speed $(\mu m \cdot s^{-1})$ | Wavelength $(\mu m)$ | Period (s) |
|---|---|---|
| 20 | 143.8 | 7.19 |
| 40 | 296.8 | 7.42 |
| 60 | 447.2 | 7.45 |
| 80 | 596.8 | 7.46 |



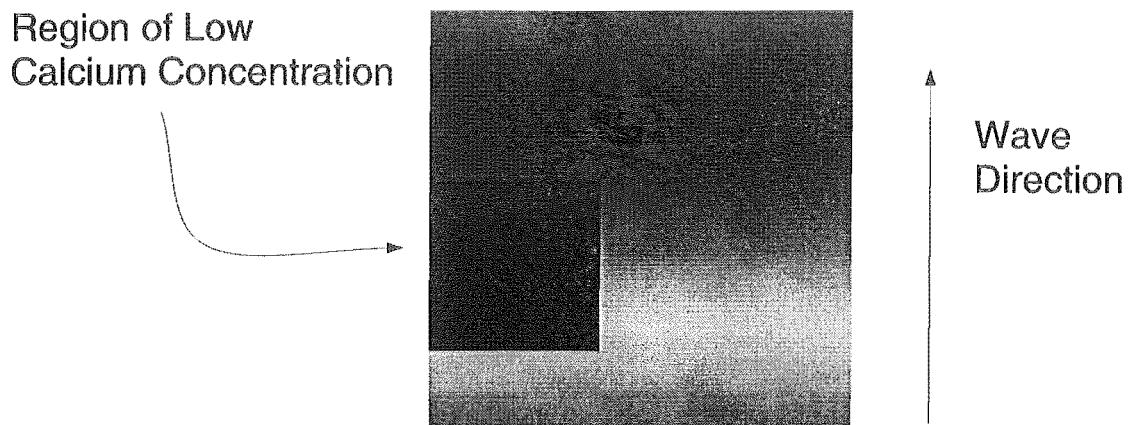Figure 18: Initial conditions for an unstable spiral wave. A periodic travelling wave is perturbed by a region within which $[Ca^{2+}]$ is held at 0.02 $\mu M$ for 10 seconds. The square size within which the simulation takes place is chosen so that a whole number of wavelengths will fit within it. The light areas represent regions of high $[Ca^{2+}]$, and the dark areas regions of low $[Ca^{2+}]$.

## 8.5 Spiral Wave Characteristics

### 8.5.1 Introduction

Unstable spirals could be formed by breaking periodic $[Ca^{2+}]$ waves of different wavelengths and periods. It was hypothesised that the spirals produced would be different in some way, in particular that their wavelengths and periods would differ. In order to test this hypothesis the spirals had to be compared in some objective manner. The characteristics of the spirals that were measured were width of the spiral arms, and the period of the spiral rotation. Because the spiral were unstable there was a limited time interval over which the characteristics could be measured. This time interval was approximately 120 seconds (16-17 rotations).

### 8.5.2 Rotation Period

During the time interval over which a spiral was stable the number of complete rotations it performed was measured. Dividing the time interval for the spiral was stable by the number of rotations it performed gives the mean rotation period for the spiral.

The start and end of a rotation were taken as the moment when the spiral tip first touched the horizontal line passing through the spiral centre (Figure 19). The spiral tip does not have a sharp edge so the moment at which it passes through the horizontal line is not precise. In addition, because the centre of the spiral is not precisely defined, then the position of the horizontal line is also not precisely defined. Therefore because the position of the horizontal line is not precise, and neither is the edge of the spiral tip, the measurement of the time interval over which the spiral was rotating has some measurement error. However, there are plausible lower and upper bounds on the position of the horizontal line, and the spiral tip boundary. Using these bounds estimates were made of the measurement error in the time intervals that were measured.

### 8.5.3 Width of Spiral Arms

When a spiral was forming or breaking up the spiral arms were indistinct. Therefore it was decided to measure the width of a spiral arm at a time approximately half way between the times of spiral formation and spiral break up.

For a given spiral, the spiral arm width varies depending where on the spiral one is. To ensure that differences in arm widths between spirals was not due to this the spiral arm width was measured at the same place for each spiral. Horizontal and vertical spiral arm widths were measured when the spiral tip passed through the vertical line going through the spiral centre (Figure 20). Like the spiral tip, the

Spiral
Centre
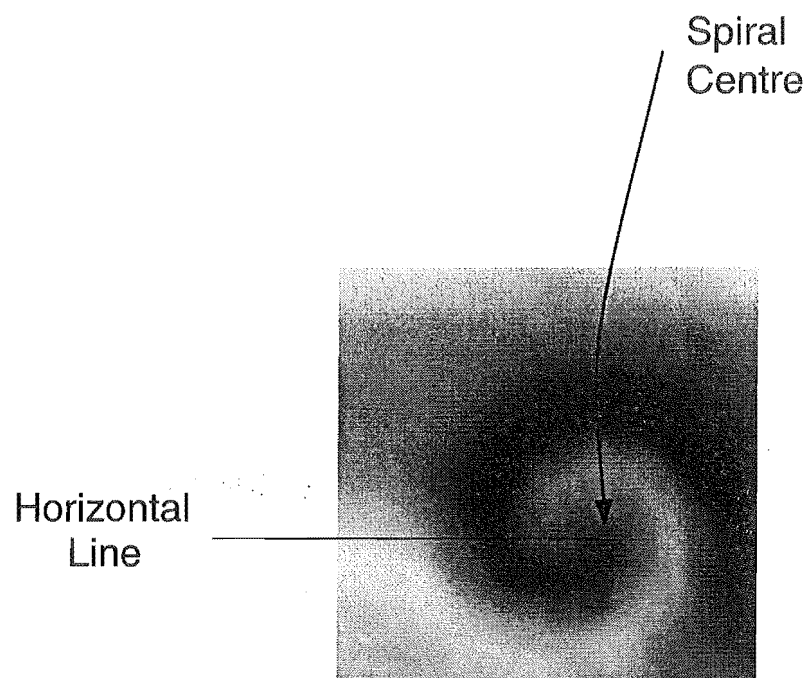
Horizontal
Line



Figure 19: Measuring the rotation period of a spiral wave. The start of a rotation is taken as the time when the spiral tip just touches a horizontal line going through the spiral centre. The return of the spiral tip to this position completes one rotation.

edge of the spiral arms is not well defined. It was decided, for consistency, to define the edge as being at the value $[Ca^{2+}] = 0.59\mu M$. This value is not arbitrary as it also appeals visually as an edge.

Because the spiral was simulated on a grid the arm widths can only be measured to a certain accuracy. Also, because the centre of the spiral is not well defined, then the positions of the horizontal and vertical lines along which the widths are measured is also not well defined. However, this was found to make a negligible contribution to the overall measurement error. Inaccuracies due to the spacing between grid points was found to be the main contributor to measurement error in the spiral arm widths. This error was estimated as being $\frac{1}{2}$ of the interval between grid points.

Figure 20: (a) Horizontal and vertical cross-sections through the centre of the spiral. (b) The width of the spiral is measured in the horizontal and vertical directions. The edge of the spiral is defined as being at $[Ca^{2+}]$ equals 100 units $(0.59\mu M)$.
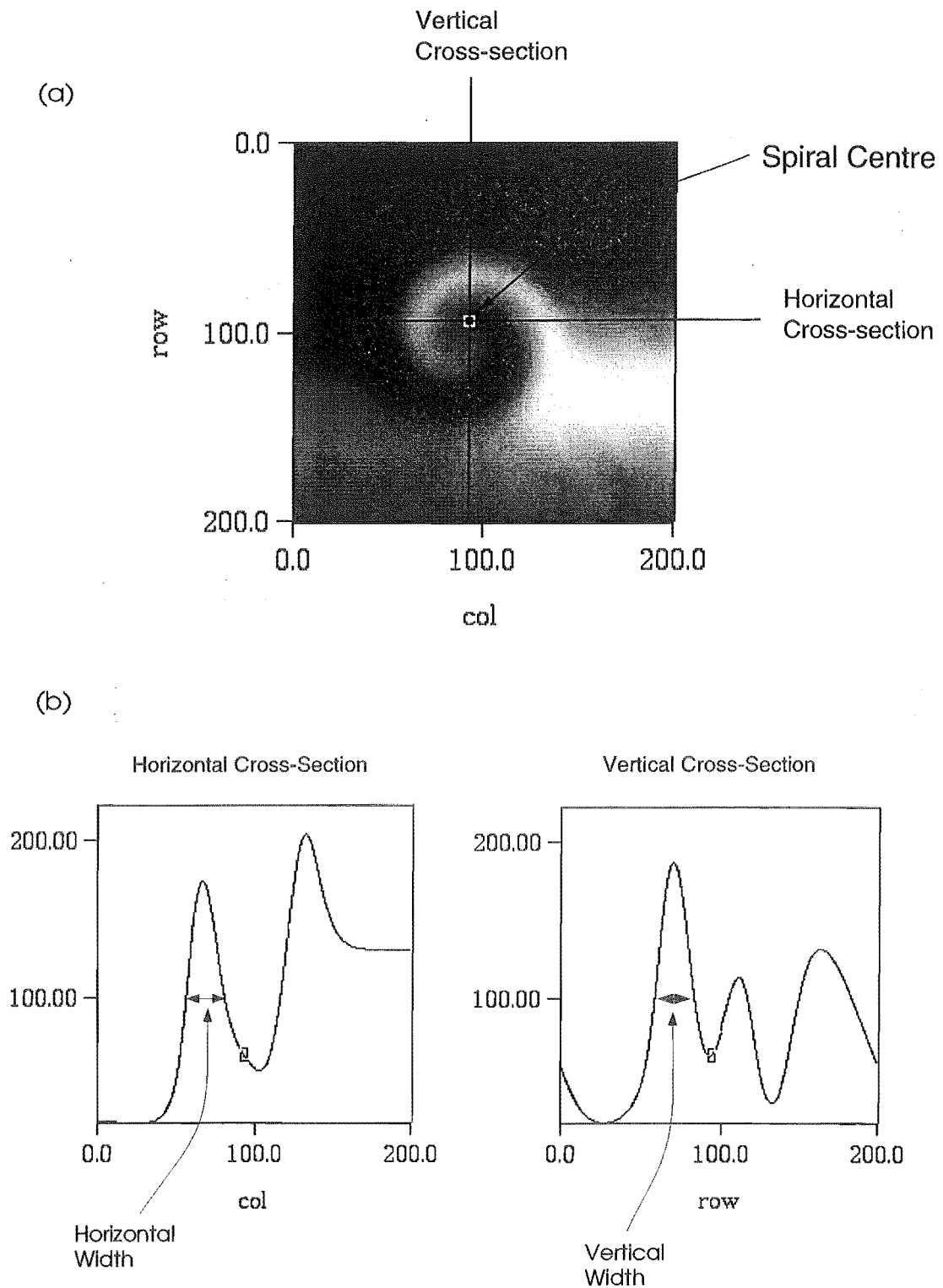
## 8.6 Results

### 8.6.1 Overview

A variety of complex phenomena other than spiral formation were observed in the simulations. Examples of such simulation behaviour included the formation of pulsating patterns, multiple spiral tips, and amorphous structures (Figure 21). These patterns occurred after a spiral formed then broke up. When a spiral broke up pulsating patterns or amorphous structures formed first, followed by multiple spiral tips.

In nearly all of the simulations a spiral formed. When a spiral formed it remained stable for approximately 120-160 seconds, then it would break up. In some of the simulations another spiral would reform after a time interval of about 80-120 seconds (Figure 22). In the long term, whether another spiral reformed or not, either amorphous structures, pulsating patterns, or multiple spiral tips formed.

### 8.6.2 Spiral Formation, Breakup, and Reformation

In nearly all of the simulations a spiral formed. In the only simulation in which a spiral did not form the cell size was $143.8\mu m$ by $143.8\mu m$, which seems to be too small for a spiral to form. Some representative simulation results are outlined in the following tables. In some simulations just a single spiral would form, then break up into irregular structures (Table 5). In many simulations, after the breakup of a spiral, another spiral would reform (Table 6). In an extreme case a spiral can reform up to seven times (Table 7). Note that an event, such as the formation of a spiral, does not occur at a particular instant in time but rather over a period of time. Hence the times given for the occurrence of events are approximate.

Table 5: Wave speed $= 20 \ \mu m \cdot s^{-1}$, wavelength $= 143.8 \ \mu m$, cell size $= 287.5 \ \mu m$ by 287.5 $\mu m$, grid size $= 200$ by 200. The boundary conditions are periodic on the top and bottom, and no flux on the left and right hand sides.

| Approximate Times (seconds) | Simulation Event |
|---:|---|
| 60 | spiral has formed |
| 190 | spiral breaks up |
| 190-300 | amorphous structures |
| >300 | pulsating patterns and multiple spirals |

Table 6: Wave speed $= 80 \ \mu m \cdot s^{-1}$, wavelength $= 596.7 \ \mu m$, cell size $= 596.7 \ \mu m$ by 596.7 $\mu m$, grid size $= 200$ by 200. The boundary conditions are periodic on the top and bottom, and no flux on the left and right hand sides.

| Approximate Times (seconds) | Simulation Event |
|---:|---|
| 70 | spiral has formed |
| 210 | spiral breaks up |
| 345 | 2nd spiral reforms at the centre |
| 450 | 2nd spiral breaks up |
| 450-630 | amorphous structures |
| >630 | multiple spirals form |

Table 7: Simulation Events: cell size = 447.15 $\mu m$ by 447.15 $\mu m$, wavelength = 447.15 $\mu m$, grid size = 200 by 200. The boundary conditions are periodic on the top and bottom, and no flux on the left and right hand sides.

| Approximate Times (seconds) | Simulation Event |
|---:|---|
| 70 | spiral forms in the centre |
| 230 | spiral breaks up |
| 340 | 2nd spiral reforms in the centre |
| 460 | 2nd spiral breaks up |
| 580 | 3rd spiral forms in the centre |
| 730 | 3rd spiral breaks up |
| 820 | 4th spiral forms in the centre |
| 960 | 4th spiral breaks up |
| 1080 | 5th spiral forms in the centre |
| 1212 | 5th spiral breaks up |
| 1530 | a weak 6th spiral forms above the centre |
| 1650 | 6th spiral breaks up |
| 1650-1800 | pulsating patterns |
| 1800 | 7th spiral forms to right of centre of square |
| 1920 | 7th spiral breaks up |
| 1920-2000 | pulsating patterns |

Spiral formation followed a similar pattern as had been observed for the stable spiral. The periodic wave was broken and bent by the refractory region of $[Ca^{2+}]$. Once the wave has been bent the curvature dependence of the wave speed maintains and increases the bending. After a time period of about 120 seconds a spiral wave formed.

However after about another 120 seconds this spiral breaks up. The process of spiral breakup was the same in all cases (Figure 23). Initially part of the central spiral arm thins, the rest of it thickening. Next, part of the inner spiral arm breaks off, but remains attached to the core by a bridge of $[Ca^{2+}]$. Eventually the part that has broken off attaches to the outer spiral arm. The part of the spiral arm that was originally attached to the central core thins until eventually it is no longer connected to the central core. The entire breakup process takes about 100 seconds.

In many cases the breakup of a spiral would be followed by the reformation of another spiral. The process of spiral reformation is a complex process (Figure 24). To start the outer spiral arm is connected to the remnants of the inner arm by a bridge of $[Ca^{2+}]$. It is unclear exactly happens to the outer arm but it appears to thin until eventually it no longer exists. possibly it is also rotating at slower speed than the inner arm, contributing to a shift in its position relative to the inner arm. As the outer arm changes size and shape the inner arm slowly reconnects to an outer circle of $[Ca^{2+}]$ to reform a spiral. Spiral reformation takes about $80 - 120$ seconds.

The boundary conditions and grid spacing had little effect on spiral formation and breakup. For comparison purposes simulations were made with no flux boundary conditions on all the sides. Simulations were also made on a 50 by 50 grid and the results compared to simulations on a 200 by 200 grid. It was found that the boundary conditions and grid spacing had little effect on spiral reformation and breakup. For example, for simulations with a wave speed of 60 $\mu m \cdot s^{-1}$ at least 3 spirals formed and broke up, irrespective of the boundary conditions and grid spacing. Furthermore, they formed and broke up at the same times. This is good evidence that the processes of spiral breakup and reformation are not artifacts of the grid size or boundary conditions.
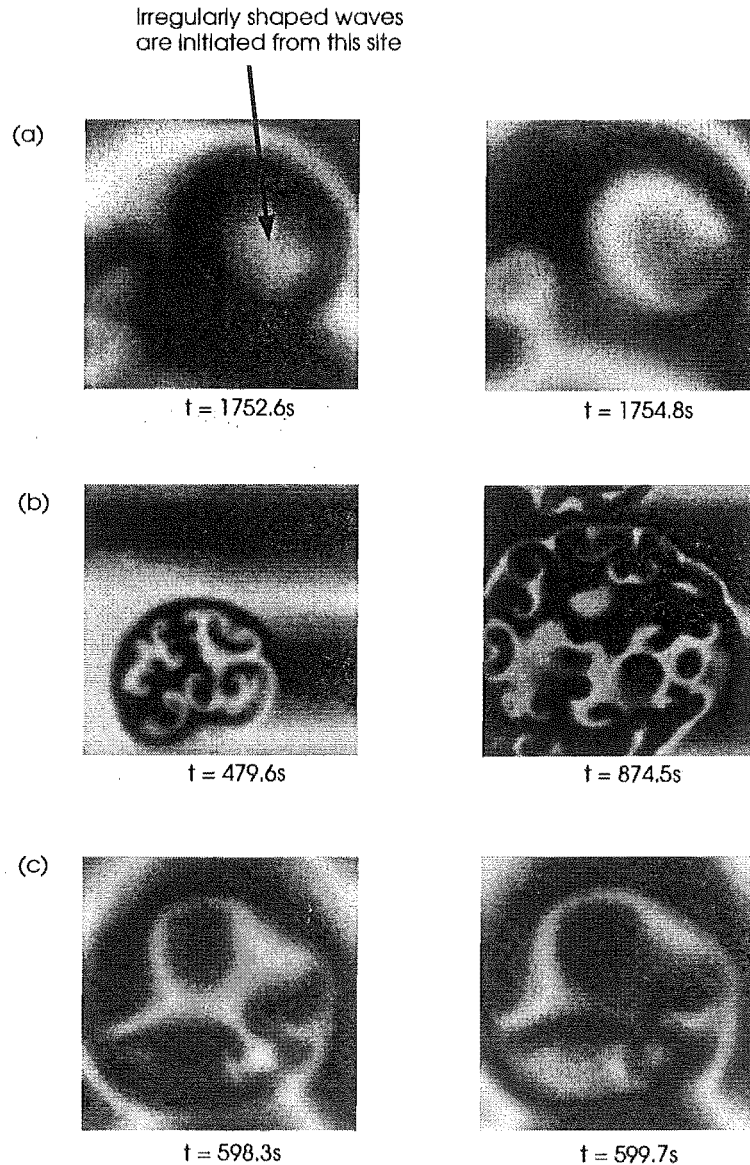
Figure 21: Some typical simulation phenomena. All grid sizes for these simulations were 200 by 200. Boundary conditions were periodic on the top and bottom, and no flux on the left and right hand sides. The initial conditions were as shown in Figure 18. The parameter value are as shown in Table 3. (a) The formation of pulsating patterns. A region periodically emits irregularly shaped waves of high $[Ca^{2+}]$ . This type of behaviour is similar to target patterns, except that the waves that form are not circular in shape. Wavelength = 447.15 $\mu m$, cell size = 447.15 $\mu m$ by 447.15 $\mu m$ (b) The formation of multiple spirals. These spread and eventually fill the entire domain. Wavelength = 596.7 $\mu m$, cell size = 1193.5 $\mu m$ by 1193.5 $\mu m$ . (c) Amorphous structures. These will often precede the formation of multiple spirals. Wavelength = 596.7 $\mu m$, cell size = 596.7 $\mu m$ by 596.7 $\mu m$ .

Figure 22: Spiral formation and breakup. Cell size $= 447.15\ \mu m$ by $447.15\ \mu m$, wavelength $= 447.15\ \mu m$, grid size $= 200$ by $200$. The boundary conditions are periodic on the top and bottom, and no flux on the left and right hand sides.The parameter value are as shown in Table 3. The light areas represent regions of high $[Ca^{2+}]$, the dark areas regions of low $[Ca^{2+}]$. (a) Initial conditions (b) A spiral begins to form near the centre (c) The spiral is fully formed (d) The spiral starts to lose shape and break up (e) Spiral breakup (f) Another spiral reforms near the centre.
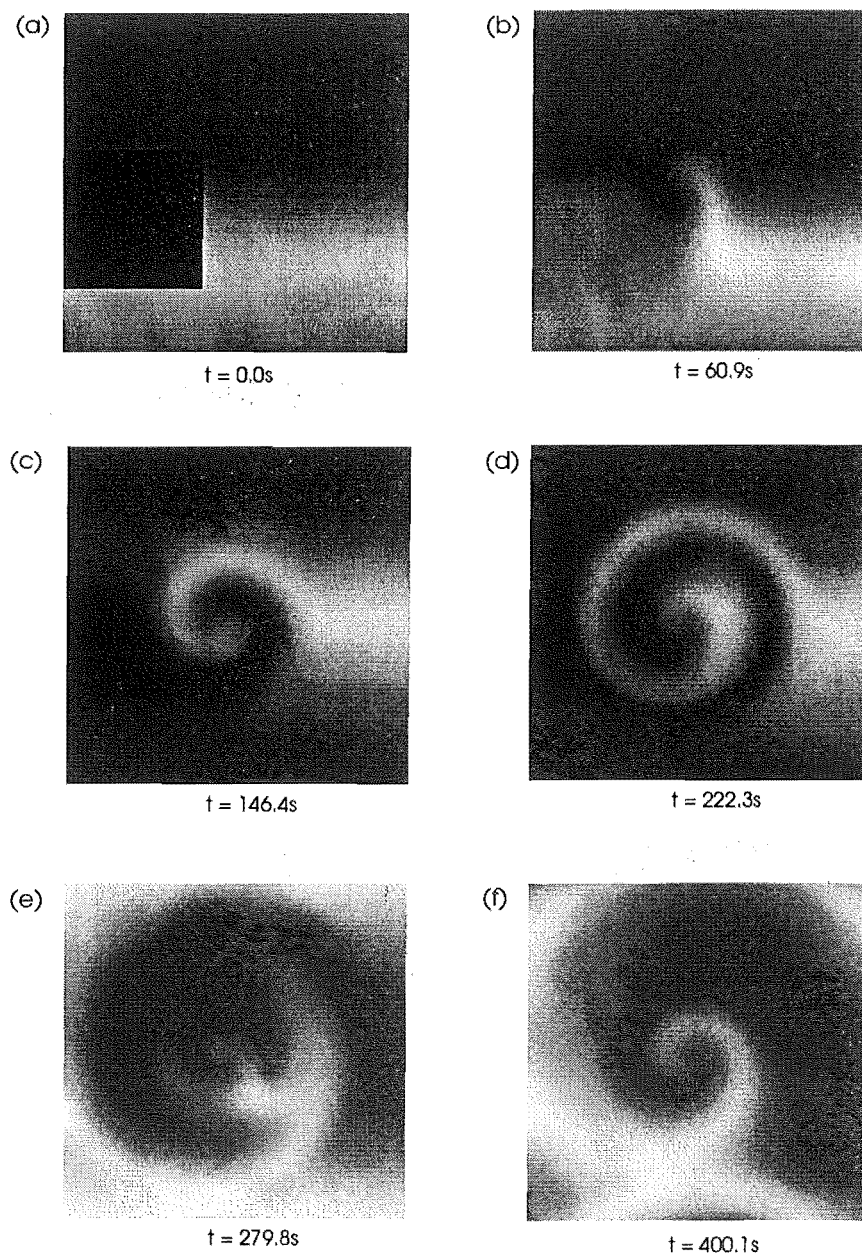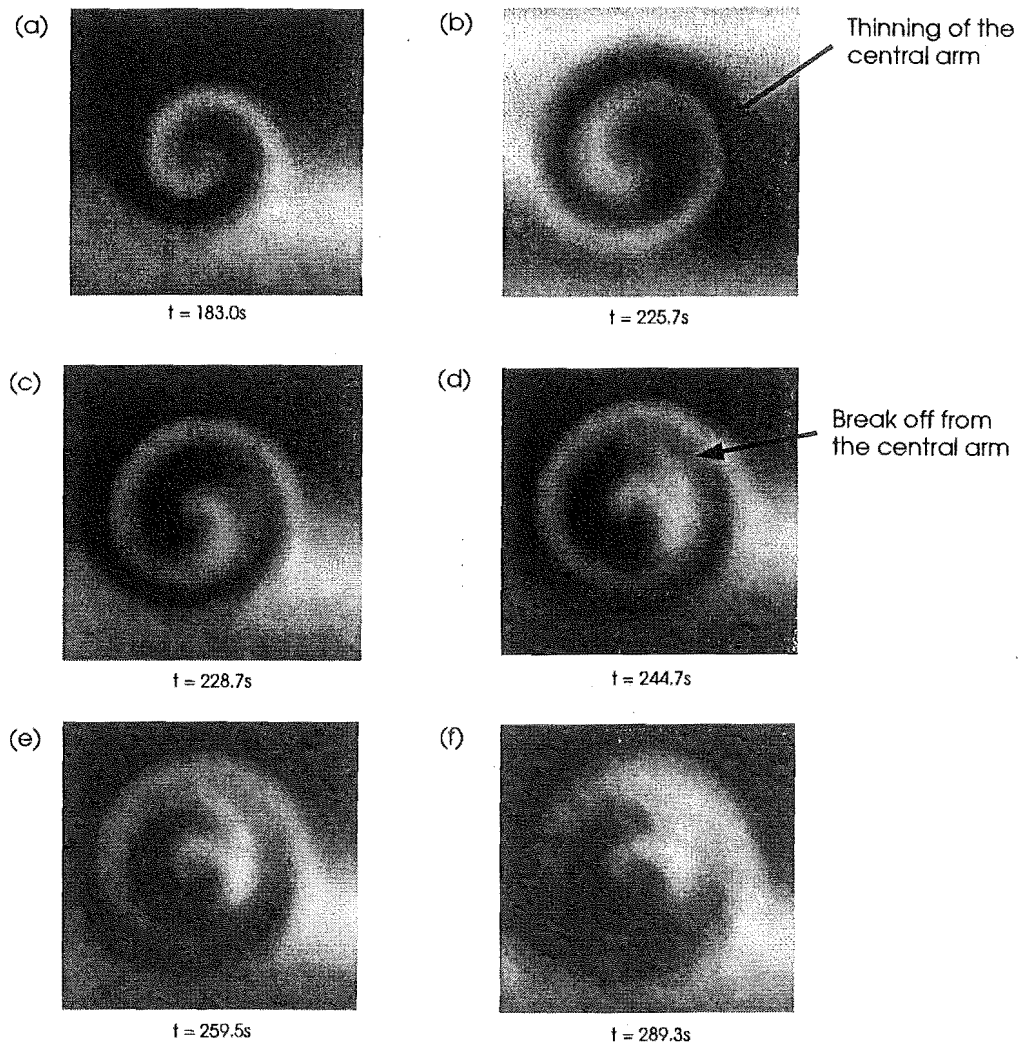
Figure 23: Spiral breakup. Cell size = 447.15 $\mu m$ by 447.15 $\mu m$, wavelength = 447.15 $\mu m$, grid size = 200 by 200. The boundary conditions are periodic on the top and bottom, and no flux on the left and right hand sides. These simulation images are from the same simulation as shown in Figure 22. The light areas represent regions of high $[Ca^{2+}]$ , the dark areas regions of low $[Ca^{2+}]$ . (a) A fully formed spiral (b) The spiral arm thins (c) The spiral arm thins further and a section of the inner spiral arm starts to break off (d) The inner and outer arms start to join (e) The inner and outer arms join (f) Further breakup of the central spiral arm. Notice that the spiral tip remains intact.
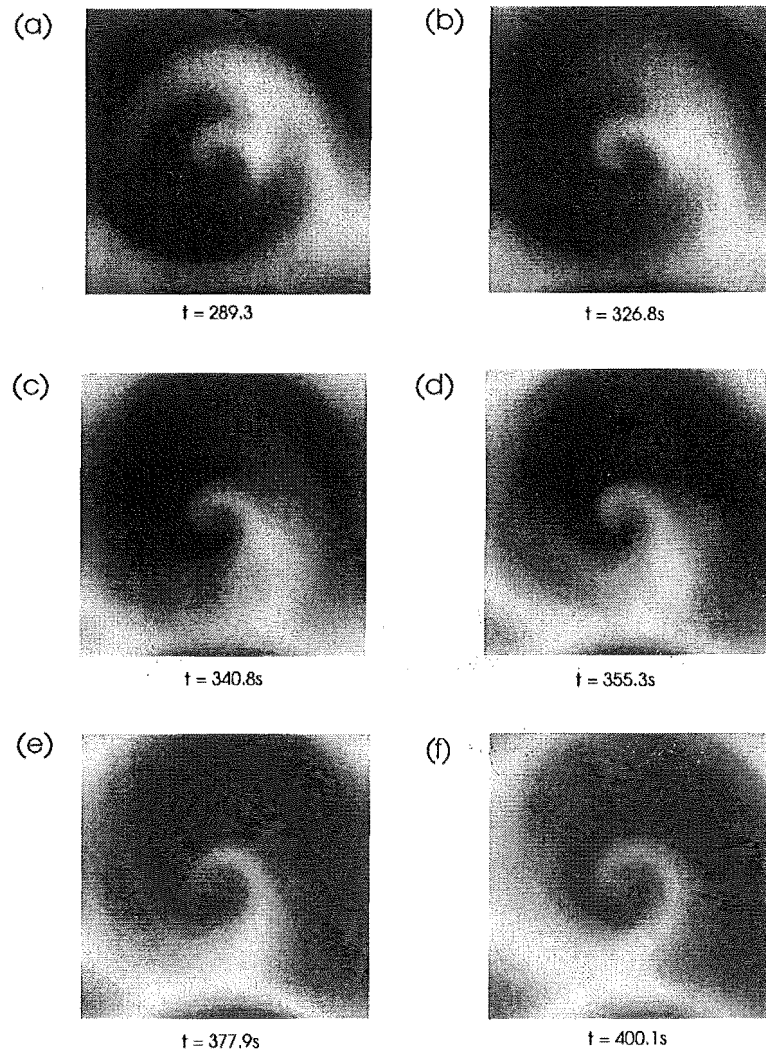
Figure 24: Spiral reformation. Cell size $= 447.15$ $\mu m$ by $447.15$ $\mu m$, grid size $= 200$ by 200, travelling wave speed $= 60$ $\mu m \cdot s^{-1}$. The boundary conditions are periodic on the top and bottom, and no flux on the left and right hand sides. This figure shows the reformation of a spiral, after the breakup of a spiral (see Figure 23). The light areas represent regions of high $[Ca^{2+}]$, the dark areas regions of low $[Ca^{2+}]$.

### 8.6.3 Characteristics of Spirals

The horizontal and vertical widths of the spirals produced did not show any significant patterns (Table 8). More specifically, they did not increase or decrease in a monotonic fashion with the speed or period of the travelling wave that initiated them. The widths of the spiral arms were the same in both the horizontal and vertical directions (Table 8).

The mean rotation period of the spiral and the period of the initial travelling wave were related. For nearly all of the simulations the period of the spiral wave was less than the the period of the initial travelling wave (Table 8). Somewhat surprisingly, the period of the spiral wave *decreased* as the period of the travelling wave *increased* (Figure 25).

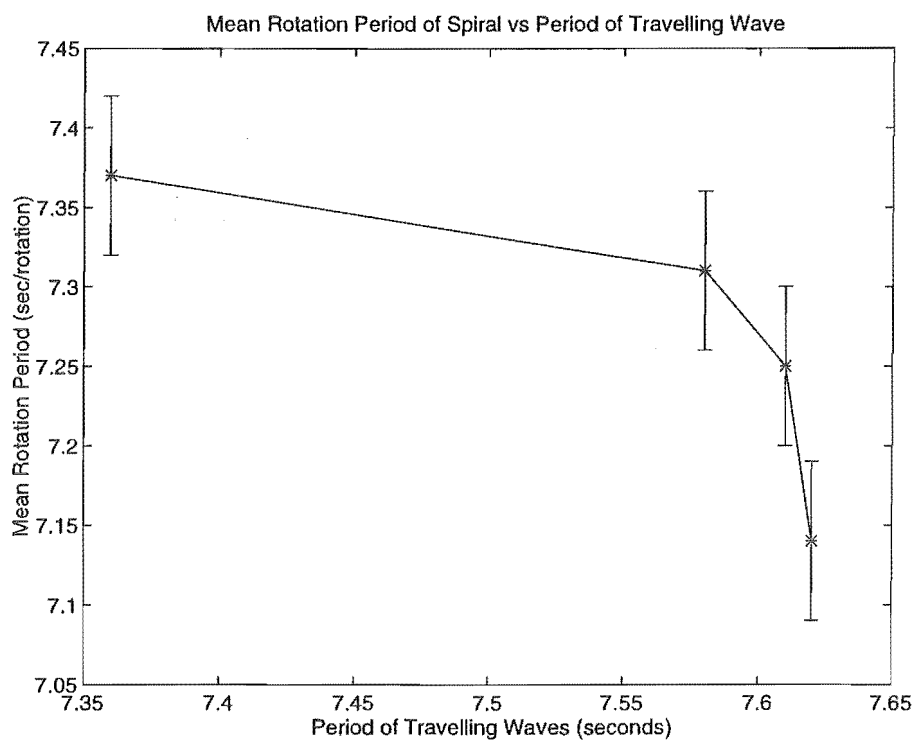Figure 25: Mean rotation period of spiral wave (seconds/rotation) vs period of travelling wave (seconds). The rotation period of the spiral was calculated as a mean over $10 - 20$ rotations. The period of the travelling wave is the actual period as measured for an unperturbed travelling wave. The vertical lines are error bars for the mean rotation period.

## 8.7 Discussion

The method used to initiate spirals was very successful; spiral wave were produced in nearly all of the simulations. However, the spirals produced were all unstable. Therefore the results can not be used to test the hypothesis that there is a unique spiral wave solution for an oscillatory system. However, despite the wide range in the wavelengths of the initial periodic waves, the arms widths of the spirals produced do not vary much. This suggests that the stable spirals might be unique. The initial periodic wave does influence the period of the spiral wave, but as the spirals that form are unstable no conclusion can be drawn regarding the stable spiral solutions from this.

However unstable spirals are of interest as in experiments with the Xenopus laevis oocyte unstable spirals are also observed. Experimentally, $[Ca^{2+}]$ waves of different period and wavelength may be set up by a line block of $IP_3$. The simulation results suggest that with the right choice of background $[IP_3]$ a line block of $IP_3$ could be used to produce unstable spirals. A comparison of the stability properties of these spirals with the model spirals could be used as a further test of the model.

Spiral breakup has been observed in a number of other models. These include cellular automata models of an evolutionary process [7], and a model for the spread of electrical activity in cardiac tissue [20]. In a continuous excitable media spiral breakup has been observed in a model for the breakup of electrical activity in cardiac tissue [22], [23] and in a modified FitzHugh-Nagumo model [40]. A variety of mechanisms have been proposed to explain spiral breakup [22],[40],[3],[32]. In the Atri model spiral breakup seems to occur when the calcium concentration contour lines start to cross. Just how this depends on the initial conditions, parameter values, and domain size is unknown. Extensive further simulations are required to characterise the dependence.

| TRAVELLING WAVE | | | | | SPIRAL WAVE CHARACTERISTICS | | |
|---|---|---|---|---|---|---|---|
| Wave Speed | Wave Wavelength | Wave Period (Act) | Cell Width | | Mean Rotation Period | Width Horizontal | Width Vertical |
| 20 | 143.8 | 7.36 | 287.5 | | 7.37 | 53.3 | 46.0 |
| 40 | 296.8 | 7.58 | 296.8 | | 7.31 | 65.1 | 68.1 |
| 60 | 447.2 | 7.61 | 447.2 | | 7.25 | 58.2 | 62.7 |
| 80 | 596.8 | 7.62 | 596.8 | | 7.14 | 56.6 | 53.6 |
| | | | | error ± | 0.05 | 2.0 | 2.0 |

Characteristics of unstable spiral waves. It had been found in some previous simulations that the travelling
nately 2.5% slower than the theoretical value. Therefore it was expected that the travelling waves in the s
onger period than the theoretical value. Wave Period (Act) is the actual period as measured for an unpert
l the simulations were done on a square grid, where 'cell width' was the length of one side. The rotation pe
ilated as a mean over 10-20 rotations. The row (error ±) is an estimate of the measurement error due to the c
al and temporal variables in the simulation. All units for distance are micrometres ($\mu m$). All units for speed
id ($\mu m \cdot s^{-1}$). The mean rotation period of the spiral has units of seconds/rotation.

# 9 Transition: Stable to Unstable Spirals

## 9.1 Introduction

With the right initial conditions and parameter values a stable spiral will form in the model equations (Section 7). This is an important result because stable spirals are observed in experiments, and it is essential to be able to reproduce this phenomenon in the model. However with other initial conditions and parameters values unstable spirals also form in model equations (Section 8). This is an important result as well because unstable spirals are also observed in experiments. So both stable and unstable spirals are observed in experiments and in the model. What is it that leads to some spirals being stable while others are unstable?

Theoretical and modelling work on one-dimensional systems suggests that the initial $[Ca^{2+}]$ concentration gradient is important. The $\lambda - \omega$ system has been used as a prototype system for studying reaction-diffusion equations. In this system it has been found that if the gradient in the initial conditions is large enough then periodic plane wave solutions destabilise into irregular patterns. This result is confirmed by simulations with the one-dimensional Atri model. In this model an $IP_3$ bolus can be used to initiate periodic calcium waves. The higher the initial $[IP_3]$ the steeper is the gradient in the $[Ca^{2+}]$ at the start of the simulations. It is found that as the initial $[IP_3]$ is increased then periodic waves destabilise into irregular waves.

These results suggest that if the $IP_3$ bolus is large enough then spiral waves in the two-dimensional Atri model may destabilise into irregular patterns. In addition, it has been found that the period of the waves in the one-dimensional Atri model decrease as the applied $IP_3$ bolus increases. This suggests that the size of the initial $IP_3$ bolus may affect the period of the spiral waves as well, most likely decreasing the period as the applied $IP_3$ bolus is increased.

## 9.2 Instability in the One-Dimensional System

### 9.2.1 Introduction

There are two ways in which spirals can be unstable [21]. The first is with regard to the position of the spiral centre. The centre may wander, or meander, but with the basic spiral shape remaining the same. The second way is with regard to the actual shape of the spiral. The shape can break up resulting in complex patterns that are suggestive of spatial-temporal chaotic behaviour.

At large distances from the spiral core the arms of a spiral wave tend to periodic plane waves. Because of this the stability properties of plane wave solutions are useful guides to the stability properties of spiral wave solutions. Much work has been done on the properties of periodic plane wave solutions to reaction-diffusion

systems of equations. A model system that has been found to be useful for such studies is the $\lambda - \omega$ system. This system is used as a prototype for studying reaction-diffusion equations that have a stable limit cycle in the kinetics. As the Atri model is of this form much can be learnt concerning its behaviour by studying the simpler $\lambda - \omega$ system.

### 9.2.2 The $\lambda - \omega$ System

The $\lambda - \omega$ system is used as a prototype for studying reaction-diffusion systems with stable oscillatory solutions for the kinetics.The $\lambda - \omega$ system takes the form

$$\frac{\partial u}{\partial t} = \frac{\partial^2 u}{\partial x^2} + \lambda(r)u - \omega(r)v, \tag{66}$$

$$\frac{\partial v}{\partial t} = \frac{\partial^2 v}{\partial x^2} + \omega(r)u + \lambda(r)v, \tag{67}$$

where $r^2 = u^2 + v^2$, and u and v are functions of space x and time t. If $\lambda(0)$ and $\omega(0)$ are both strictly positive, and $\lambda(r)$ has a isolated positive root $r_L$, then the kinetics have a stable limit cycle solution. These equations have a one-parameter family of periodic plane wave solutions given by

$$u = \hat{r}cos[\omega(\hat{r})t \pm \omega(\hat{r})^{\frac{1}{2}}x], \tag{68}$$

$$v = \hat{r}sin[\omega(\hat{r})t \pm \omega(\hat{r})^{\frac{1}{2}}x], \tag{69}$$

where $0 < \hat{r} < r_L$ [27] . These solutions are linearly stable if and only if

$$4\lambda(\hat{r}) + \left[1 + \left(\frac{\omega'(\hat{r})}{\lambda'(\hat{r})}\right)^2\right] + \hat{r}\lambda'(\hat{r}) \le 0. \tag{70}$$

If the waves are of sufficiently low amplitude they are unstable, while those of high amplitude are stable.

A particular instance of these equations has

$$\lambda(r) = \lambda_0 - r^p, \tag{71}$$

$$\omega(r) = \omega_0 - r^p, \tag{72}$$

with initial conditions $u(x,0) = v(x,0) = Ae^{(-\xi x)}$ and boundary conditions $u, v \to 0$ as $x \to \infty$, and $u_x = v_x = 0$ at $x = 0$. These initial conditions give, in the long term, periodic wave solutions with a particular speed and amplitude, these being determined by the value of $\xi$ [47]. The periodic wave solutions have an amplitude

$$r_0 = \left[ \frac{1}{2}(\sqrt{s^4 + 4s^2\lambda_0} - s^2) \right]^{\frac{1}{p}} \tag{73}$$

and a speed given by

$$c_{pw} = \frac{-\omega(r_0)c}{\omega_0 - \omega(r_0)} \tag{74}$$

where

$$c = \begin{cases} \xi + \lambda_0/\xi, & 0 < \xi \leq \sqrt{\lambda_0} \\ 2\sqrt{\lambda_0}, & \xi \geq \sqrt{\lambda_0} \end{cases} \tag{75}$$

These periodic wave solutions are stable if

$$r_0 > [8\lambda/(8+p)]^{\frac{1}{p}}. \tag{76}$$

Thus depending on the value of $\xi$, different periodic wave solutions result. It is found that as $\xi$ increases the speed of the wave decreases, as does the amplitude. If the amplitude becomes small enough the periodic wave destabilises and irregular oscillations are observed. Or to state this in another way, as $\xi$ increases the gradient in the initial conditions increases, and periodic wave solutions destabilise.

### 9.2.3 The One-Dimensional Atri Model

The one-dimensional Atri model is, like the $\lambda - \omega$ system, a reaction-diffusion system whose kinetics have a stable limit cycle solution. Therefore it is expected that periodic wave solutions in the Atri model will also destabilise if the gradient in the initial conditions is large enough. Simulations with the one-dimensional version of the Atri model confirm this conclusion [49]. A bolus of $[IP_3]$ may be used to initiate periodic calcium waves. The larger the initial $[IP_3]$ bolus then the greater the initial gradient in the $[Ca^{2+}]$. If the $[IP_3]$ is large enough then, after a sufficiently long time, periodic wave solutions destabilise and take on an irregular profile. Furthermore it is found that the period of the waves decreases as the size of the initial $IP_3$ bolus is increased.

## 9.3 Method

Studies with the $\lambda - \omega$ system and the one-dimensional Atri model suggest that a high enough initial $IP_3$ bolus will result in the destabilisation of spiral wave solutions. Changing the $IP_3$ bolus may also affect the period of the spirals that form. A simple change to the initial conditions used to generate a stable spiral can be used to test this hypothesis.

Exactly the same parameter values, boundary conditions, and geometry were used as in section 7, except that the size of the $[IP_3]$ bolus was varied. A initial $[IP_3]$ bolus size from $1\mu M$ up to $35\mu M$ was used. The simulations were then run for up to 3000 seconds to see whether or not a spiral wave formed, and if it was stable. If the spiral broke up the length of time for which it remained stable was recorded. The period of each spiral was measured, a mean being taken over the first 10-20 rotations (Section 8.5.2).

Also recorded was the long term $[IP_3]$ and the corresponding $\mu$ value. When the initial $IP_3$ bolus is released $IP_3$ rapidly diffuses through the square. Within a short time ($\approx$ 50-100s) the $[IP_3]$ is nearly constant throughout the square, the concentration approaching a long term $[IP_3]$. Corresponding to the long term $[IP_3]$ is a bifurcation parameter $\mu$ value set by equation 16. The long term $[IP_3]$ and corresponding $\mu$ value were recorded for each simulation.

## 9.4 Results

### 9.4.1 Stability

The larger the initial $[IP_3]$ bolus the less time the spiral wave remains stable for (Table 9). Below an initial $IP_3$ bolus of about 30.0 $\mu M$ the spirals are stable, or at least they last for a very long time. Above this value there is a very sharp transition to unstable spirals. The spirals break up to form either pulsating patterns or more commonly multiple spiral tips. Notice that the corresponding $\mu$ value (0.3867) at the transition is well into the oscillatory regime for the system ($0.29 < \mu < 0.50$). If the initial $[IP_3]$ is below about $2\mu M$ ($\mu = 0.312$) then a stable double spiral forms (Figure 26).

If the $\mu$ is greater than 0.3867 the spiral waves starts to exhibit meander - the spiral core moves. This was a very slow anti-clockwise motion with the spiral core moving slightly closer to the boundary. For example, for an initial $IP_3$ bolus of $30\mu M$, the spiral core moved $90°$ anti-clockwise in about 1000 seconds. Reformation of spiral waves was also observed, but only if the $\mu$ value was greater than about 0.3867. For instance, with an initial bolus of $30.2\mu M$, an initial spiral forms but breaks up after about 680 seconds. However, about 200 seconds latter a double spiral forms. Within a short time ($\approx$ 200 seconds), one of the spirals grows, leaving a single spiral located at the centre of the square. This spiral is stable for a least 1500 seconds (Figure 27). If the $IP_3$ bolus at the start of the simulation is slightly higher, say $30.7\mu M$, then the long term results of the simulation are multiple spiral tips, not a single stable spiral.
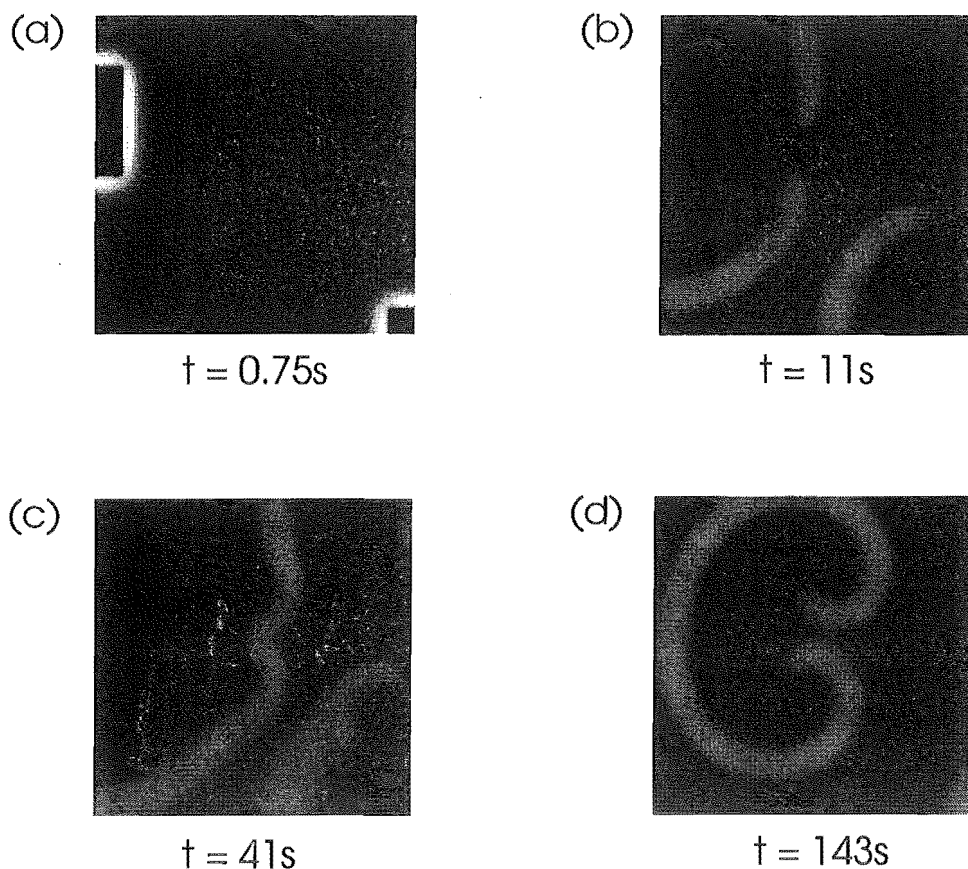
Figure 26: The formation of a stable double spiral. Initial $[IP_3] = 1.0\mu M$. Cell size = 250 $\mu m$ by 250 $\mu m$ , grid size = 240 by 240 . The boundary conditions are no flux. The parameter values for the simulation are given in Table 1. The light areas represent regions of high $[Ca^{2+}]$ , the dark areas regions of low $[Ca^{2+}]$ . (a) Initial conditions. The black rectangles are regions with a low $[Ca^{2+}]$ . The white outlined rectangles mark the two areas with an above steady state $[IP_3]$. See Figure 13 for more details on the initial conditions. (b) The regions with an initial above steady state $[IP_3]$ initiate travelling $[Ca^{2+}]$ waves. (c) A double spiral starts to form near the centre, and a single spiral starts to form near the bottom right hand corner. (d) The double spiral increases in size, dominating the single spiral. The double spiral is stable up to at least t = 3000 seconds.
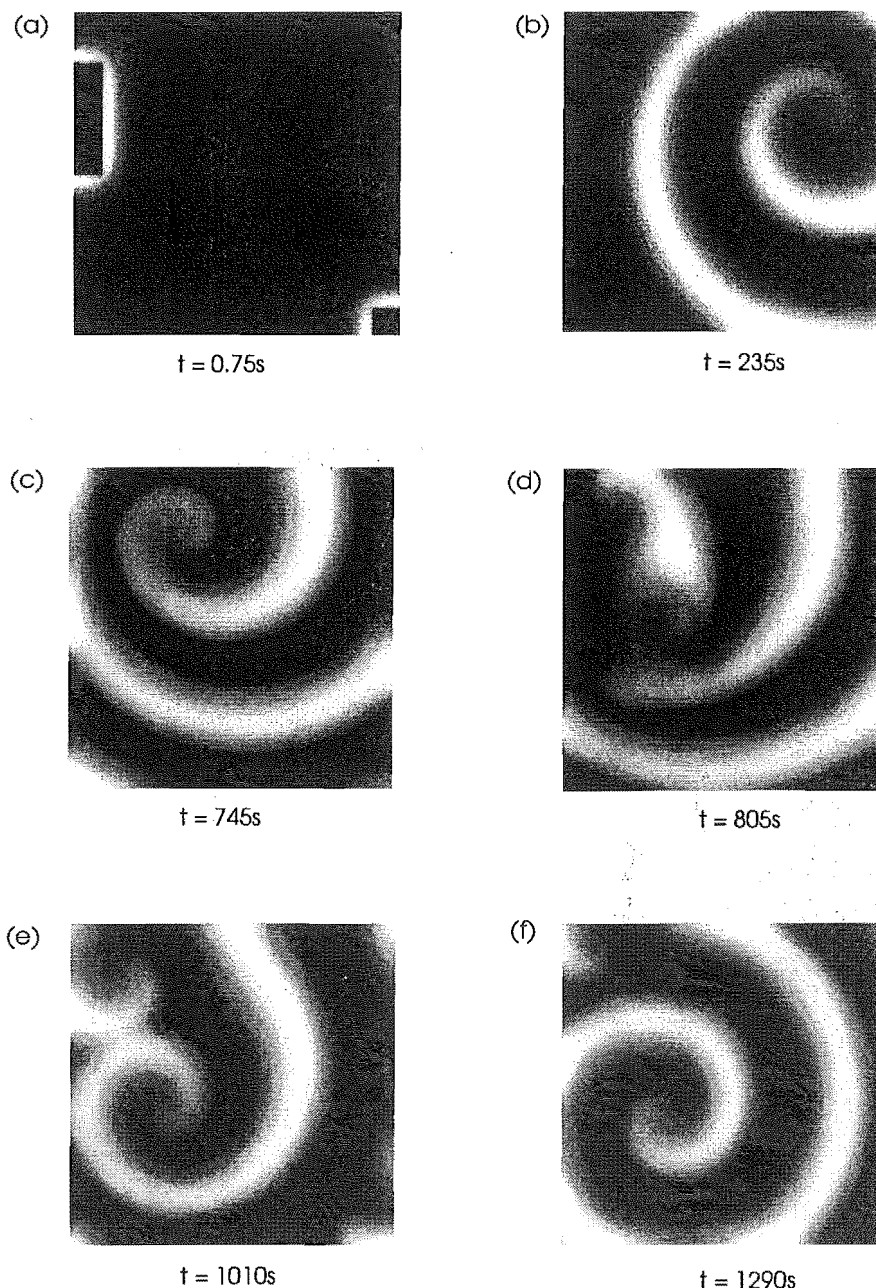
Figure 27: The reformation of a spiral. Initial $[IP_3]$ = $30.2\mu M$. Cell size = 250 $\mu m$ by 250 $\mu m$ , grid size = 240 by 240 . The boundary conditions are no flux. The parameter values for the simulation are given in Table 1. The light areas represent regions of high $[Ca^{2+}]$ , the dark areas regions of low $[Ca^{2+}]$ . (a) Initial conditions. The black rectangles are regions with a low $[Ca^{2+}]$ . The white outlined rectangles mark the two areas with an above steady state $[IP_3]$. See Figure 13 for more details on the initial conditions. (b) A single spiral forms. (c) The spiral moves along the boundary of the domain. (d) Eventually the spiral breaks up. (e) Two spirals form near where the spiral broke up. (f) The spiral nearer the centre dominates the other spiral. The single spiral that remains is stable up to at least t = 3000 seconds, and does not move.

Table 9: Different initial $[IP_3]$ conditions for the simulations. $IP_3$ diffuses through the square giving a constant, long term $[IP_3]$. Corresponding to this constant $[IP_3]$ value is a $\mu$ value. Stability is the length of time, in seconds, for which the spiral wave remained stable. The notation > 3000 means that the simulation was run up to 3000 seconds and the spiral was not observed to break up.

| Initial $[IP_3](\mu M)$ | Long Term $[IP_3](\mu M)$ | $\mu$ value | Stability (s) |
|---|---|---|---|
| 1.0 | 0.063 | 0.295 | > 3000 |
| 5.0 | 0.317 | 0.312 | > 3000 |
| 10.0 | 0.634 | 0.331 | > 3000 |
| 20.0 | 1.268 | 0.362 | > 3000 |
| 30.0 | 1.902 | 0.3867 | > 3000 |
| 30.1 | 1.908 | 0.3869 | 960 |
| 30.2 | 1.915 | 0.3871 | 680 |
| 30.4 | 1.927 | 0.388 | 230 |
| 31.5 | 1.997 | 0.390 | 125 |

## 9.4.2 Period

The period of the spiral waves decreased as the initial $[IP_3]$ bolus was increased (Figures 28 and 29). When the period is below about 7.9 seconds/rotation the spiral wave that forms is unstable. The period of the unstable spiral waves was not constant, but decreased with time at the onset of spiral break up (Figure 30).
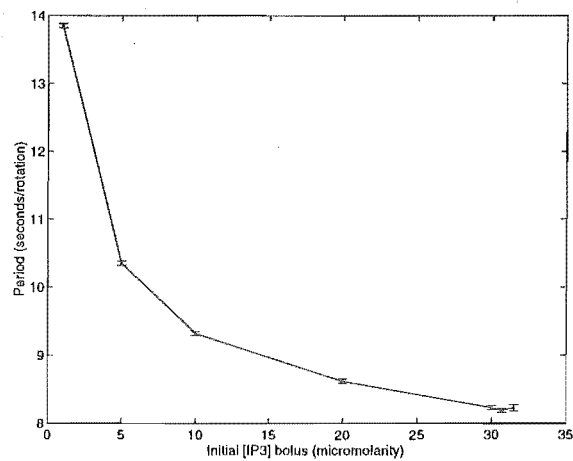
Figure 28: Initial period (seconds/rotation) of unstable spiral versus long term $[IP_3]$. When the initial period is below about 8.3 seconds/rotations the spiral wave is unstable. The period is calculated as mean over 10-20 rotations. The vertical lines are error bars. Initially $IP_3$ is localised to rectangular blocks. Within a short time (50-100 seconds) it spreads through out the domain, giving a homogeneous long term $[IP_3]$. When the long term $[IP_3]$ is greater than 1.902 $\mu M$ the spiral wave destabilises
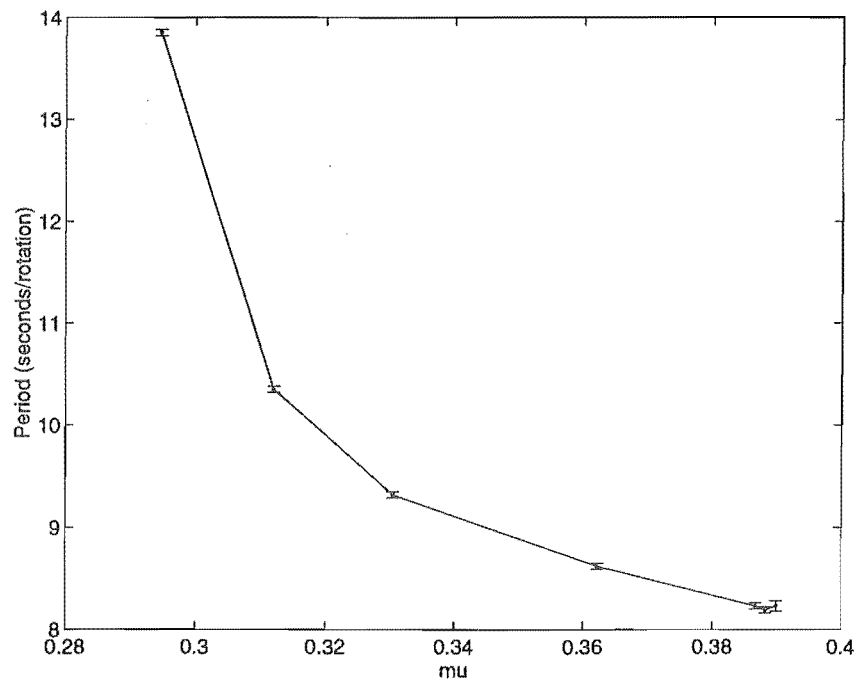
Figure 29: Period (seconds/rotation) of spiral waves versus $\mu$. The period is calcu-
lated as a mean over 10-20 rotations. The vertical lines are error bars. Initially $IP_3$
is localised to rectangular blocks. Within a short time (50-100 seconds) it spreads
through out the domain, giving a homogeneous long term $[IP_3]$. The long term $IP_3$
is used to calculate the $\mu$ value. When the $\mu$ value is greater than 0.3867 the spiral
destabilises.
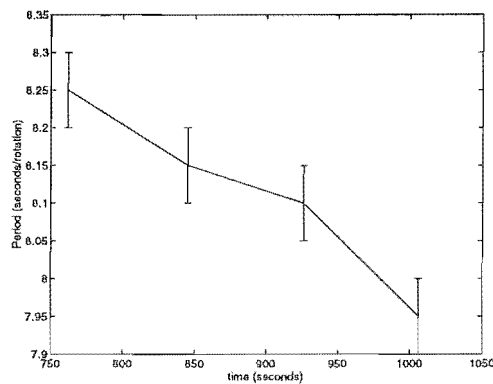
Figure 30: The decreasing period of an unstable spiral. The period of an unstable spiral decreases until it reaches a critical value of 7.9 seconds/rotation. When the critical value is reached the spiral breaks up. The period is calculated as a mean over 10 rotations, with the vertical lines measuring the uncertainty in this. The time coordinate is the midpoint of the time interval over which 10 rotations was taken. The initial $IP_3$ bolus for this simulation was $30.1\mu M$, and the spiral that formed broke up at approximately $t = 1050$ seconds.

## 9.5 Discussion

If the initial $[IP_3]$ is increased then the spiral wave is destabilised, and its period decreases. Previous work with the $\lambda - \omega$ system and the one-dimensional Atri system indicate that it is the initial $[Ca^{2+}]$ gradient that is important in determining the stability, this gradient being set up by the initial $[IP_3]$. An alternative hypothesis is that it is not the initial $[IP_3]$ that determines the stability, but instead the long term $[IP_3]$. If the long term $[IP_3]$ is low enough then the spirals will be stable. One way to test this hypothesis would be to do some further simulations with a higher initial background $[IP_3]$, but a lower initial $IP_3$ bolus. If the long term $IP_3$ at which the spirals become unstable is still the same as in previous simulations then it, rather then the gradient in the initial $[Ca^{2+}]$, would be determined as the factor influencing the stability of the spirals.

A meandering spiral exhibits what is called the Doppler effect. Because of the motion of the spiral core sites ahead of the spiral core motion exhibit a period that is shorter than the true period. Sites behind the motion of the spiral core exhibit a longer period. This can led to the wave fronts of the spiral becoming unstable and the eventual break up of a spiral [3]. Thus, via the Doppler effect, spiral meander can led to spiral break up. However it is unlikely that spiral meander is the cause of spiral break up in the Atri model. While meander is observed before spiral break up, the rate of meander is very slow (90° in 1000 seconds). In addition, spiral break up also occurs when periodic plane waves are used as initial conditions, but no meander takes place in this case (Section 8).

The unstable spirals that formed showed a decrease in their period prior to break up. Once the period was less than a critical value of about 7.9 seconds/rotation they broke up. Other models, such as the Noble model for cardiac tissue, also have a critical value for the rotation period [22]. As in the Noble model, the critical value for the Atri model is expected to depend on the the parameter values for the model, and perhaps the cell size.

As the rotation period of the unstable spirals decreased the spirals simultaneously drifted along the boundaries of the simulation. Previous simulations with no-flux boundary conditions have also exhibited spiral drift along the boundary [63]. In some models for the Belousov-Zhabotinskii reaction the spirals that develop are observed to become more tightly wound and with shorter period as the simulation progresses [5],[4],[26].

A pertinent feature of the stable spirals that formed was that they had different rotation periods, the period depending on the initial $[IP_3]$. Therefore there is not a unique stable spiral solution for the system. Instead there are many possible solutions with different periods, the particular solution appearing depending on both the parameter values and initial conditions.

# 10  Conclusion

Sprial waves, both stable and unstable, can form in the oscillatory regime of the Atri model. The stable spirals that form in the oscillatory regime are not unique. Their period depends on not only the parameters of the model, but also on the initial conditions for $IP_3$. The initial conditions for $IP_3$ also influence the stability of spiral waves: if the initial $IP_3$ bolus is high enough then the spirals destabilise.

The process of spiral breakup seems to be the same no matter what initial conditions are used in the simulations. After spiral break up a number of different events occurred. Often a spiral would break up, then latter reform again. More commonly amorphous structures would form, these eventually been followed by multiple spiral tip behaviour.

# A Physical Model for the $IP_3$ Receptor

It is known that release of $Ca^{2+}$ from the IPR is dependent on both $[Ca^{2+}]$ and $[IP_3]$. Furthermore, the efflux of $Ca^{2+}$ is known as a function of the steady state $[Ca^{2+}]$ [41]. A simple physical model [2] can reproduce these observations, and is useful as a guide to understanding . For a more detailed receptor model see DeYoung and Keizer [11].

## A.1 The Model

It is known a $Ca^{2+}$ efflux is activated by the binding of $Ca^{2+}$ and $IP_3$ to the IPR. For simplicity consider a single IPR channel, and assume that it has three independent binding domains. Let domain 1 be a binding domain for $IP_3$, and domains 2 and 3 binding domains for $Ca^{2+}$. Domain 1 is assumed to bind one $IP_3$ molecule, domain 2 one $Ca^{2+}$ ion complex, and domain 3 to bind two $Ca^{2+}$ complexes.

The receptor channel releases $Ca^{2+}$ if domains 1 and 2 are activated, but domain 3 is inactive. Therefore $IP_3$ is essential for channel activation, but $Ca^{2+}$ can activate or inactivate the receptor channel depending on the activation configuration of domains 2 and 3.

Let $p_1$, $p_2$, $p_3$ be the probability that domain 1 is activated, domain 2 is activated, and domain 3 is *not* activated. Then the probability that the IPR receptor channel is open is $p_1 p_2 p_3$. If the $Ca^{2+}$ current when a single receptor channel is open is $i$ (units of $\mu C \cdot s^{-1}$), and there are N channels, then the total IPR current is

$$I = Nip_1p_2p_3. \tag{77}$$

Let U be element of volume through which the current is flowing. If this is constant then the $Ca^{2+}$ current can be converted to a concentration flux $J_{channel}$ such that

$$J_{channel} = \frac{Nip_1p_2p_3}{2FU}, \tag{78}$$

where F is Faraday's constant, and has units of coulombs per mole. Or after letting $k_{flux} = Ni/(2FU)$ then

$$J_{channel} = k_{flux}p_1p_2p_3, \tag{79}$$

where the units of $k_{flux}$ are $\mu M \cdot s^{-1}$.

For cooperative kinetics

$$p_1 = \frac{P}{k_\mu + P} \tag{80}$$

$$p_2 = b + \frac{V_1 c}{k_1 + c} \tag{81}$$

$$p_3 = 1 - \frac{c^2}{k_2^2 + c^2}. \tag{82}$$

Therefore

$$J_{channel} = k_{flux}\mu(P) \left(b + \frac{V_1 c}{k_1 + c}\right) \left(1 - \frac{c^2}{k_2^2 + c^2}\right) \tag{83}$$

where

$$\mu(P) = \frac{P}{k_\mu + P}. \tag{84}$$

# References

[1] N.L. Allbritton, T. Meyer, and L. Stryer. Range of messenger action of calcium ion and inositol 1,4,5-trisphosphate. *Science*, 258:1812–1815, 1992.

[2] A. Atri, J. Amundson, D. Clapham, and J. Sneyd. A single-pool model for intracellular calcium oscillations and waves in the Xenopus laevis oocyte. *Biophysics*, 65:1727–1739, October 1993.

[3] M. Bär and M. Eiswirth. Turbulence due to spiral breakup in a continuous excitable medium. *Phys. Rev E*, 48(3):1635–1637, 1993.

[4] D. Barkley. Spiral meandering. In R. Kapral and K. Showalter, editors, *Chemical waves and patterns*, pages 163–188. Kluwer, Amsterdam, 1994.

[5] D. Barkley and I. Kevrekidis. A dynamical systems approach to spiral wave dynamics. *Chaos*, 4:453–460, 1994.

[6] B.Knox, P.Ladiges, and B.Evans. *Biology*, pages 30–33. McGraw-Hill Book Company, Sydney, 1994.

[7] M.C. Boerlijst and P. Hogeweg. Spiral wave structure in pre-biotic evolution: hypercycles stable against parasites. *Physica D*, 48:17–28, 1991.

[8] M.S. Bretscher. The molecules of the cell membrane. *Scientific American*, 253(4):86–90, 1985.

[9] D.E. Clapham. Calcium signaling. *Cell*, 80:259–268, January 1995.

[10] K.S. Cutherbertson and T.R. Chay. Modelling receptor-controlled intracellular calcium oscillations. *Cell Calcium*, 12:97–109, 1991.

[11] G.W. DeYoung and J. Keizer. A single pool $IP_3$-receptor based model for agonist stimulated $Ca^{2+}$ oscillations. *Proc. Natl. Acad. Sci. USA*, 89:9895–9899, 1992.

[12] P.A. Diliberto, X.F. Wang, and B. Herman. Confocal imaging of $Ca^{2+}$ in cells. In Richard Nuccitelli, editor, *A Practical Guide to the Study of Calcium in Living Cell*, volume 40 of *Methods in Cell Biology*, chapter 10, pages 243–262. Academic Press Inc., San Diego, California, 1994.

[13] L. Edelstein-Keshet. *Mathematical Models in Biology*, pages 498–509. Random House, New York, 1988.

[14] W.H. Evans and J.M. Graham. *Membrane Structure and Function*, pages 31–50. Oxford University Press, Oxford, England, 1989.

[15] E.A. Finch, T.J. Turner, and S.M. Goldin. Calcium as a coagonist of inositol 1,4,5-trisphosphate-induced calcium release. *Science (Washington DC)*, 252:442–446, 1991.

[16] S. Girard and D.E. Clapham. Simultaneous near ultraviolet and visible excitation confocal microscopy of calcium transients in *xenopus* oocytes. In R. Nuccitelli, editor, *A Practical Guide to the Study of Calcium in Living Cell*, volume 40 of *Methods in Cell Biology*, chapter 11, pages 263–284. Academic Press Inc., San Diego, California, 1994.

[17] R.A. Gray and J.Jalife. Spiral waves and the heart. *International Journal of Bifurcation and Chaos*, 6(3):415–435, 1996.

[18] P. Hausen and M. Riebesell. *The Early Development of Xenopus Laevis*, pages 19–20. Springer-Verlag, Heidelberg, 1991.

[19] C.W. Heizmann and W. Hunziker. Intracellular calcium-binding proteins: more sites than insights. *Trends Biochem. Sci.*, 16:98–103, 1991.

[20] H.Ito and L.Glass. Spiral breakup in a new model of discrete excitable media. *Phys. Rev. Lett*, 66:671–674, 1991.

[21] R. Kapral. Pattern formation in chemical systems. *Physica D*, 86:149–157, 1995.

[22] A. Karma. Spiral breakup in model equations of action potential propagation in cardiac tissue. *Physical Review Letters*, 71(7):1103–1106, 1993.

[23] A. Karma. Electrical alternans and spiral wave breakup in cardiac tissue. *Chaos*, 4(3):461–472, 1994.

[24] B.K. Kay and H.B. Peng. Preface. In Brian K. Kay and H. Benjamin Peng, editors, *Xenopus laevis: Practical Uses in Cell and Molecular Biology*, volume 36 of *Methods in Cell Biology*, pages xix–xxii. Academic Press Inc., San Diego, California, 1991.

[25] J. Keener and J.Sneyd. Mathematical physiology. Unpublished book.

[26] M. Kness, L. Tuckerman, and D. Barkley. Symmetry-breaking bifurcations in one-dimensional excitable media. *Phys. Rev. A*, 46:5054–5062, 1992.

[27] N. Kopell and L.N. Howard. Plane wave solutions to reaction-diffusion equations. *Stud. Appl. Math.*, 52:291–328, 1973.

[28] J. Lechleiter, S. Girard, D. Clapham, and E. Peralta. Subcellular patterns of calcium release determined by G protein-specific residues of muscarinic receptors. *Nature*, 350:505–508, April 1991.

[29] J. Lechleiter, S. Girard, E. Peralta, and D. Clapham. Spiral calcium wave propagation and annihilation in Xenopus laevis oocytes. *Science*, 252:123–126, April 1991.

[30] J.D. Lechleiter and D.E. Clapham. Molecular mechanisms of intracellular calcium excitability in X. laevis oocytes. *Cell*, 69:283–294, April 1992.

[31] L.Glass. Dynamics of cardiac arrhythmias. *Physics Today*, pages 40–45, August 1996.

[32] M. Markus, G. Kloss, and I. Kusch. Disordered waves in a homogeneous, motionless excitable medium. *Nature*, 371:402–404, 1994.

[33] T. Meyer and L.Stryer. Calcium spiking. *Annu. Rev. Biophys. Chem*, 20:153–174, 1991.

[34] N.G. Morgan. *Cell Signalling*, chapter 3, pages 35–57. The Guilford Press, New York, 1989.

[35] S.C. Müller, T. Plesser, and B. Hess. The structure of the spiral core in the Belousov-Zhabotinskii reaction. *Science*, 230:661–663, 1985.

[36] J.D. Murray. *Mathematical Biology*, pages 343–356. Springer-Verlag, New York, 1989.

[37] J.D. Murray. *Mathematical Biology*, pages 179–198. Springer-Verlag, New York, 1989.

[38] E. Neher and G.J. Augustine. Calcium gradients and buffers in bovine chromaffin cells. *J. Physiol (Lond)*, 450:273–301, 1992.

[39] P.C. Newell. Attraction and adhesion in the slime mould *dictyostelium*. In J.E. Smith, editor, *Fungal Differentiation: A Contemporary Synthesis*, volume 43 of *Mycology Series*, pages 43–71. Marcel Dekker, New York, 1983.

[40] A. Panfilov and P. Hogeweg. Spiral breakup in a modified FitzHugh-Nagumo model. *Physics Letters A*, 176:295–299, 1993.

[41] J.B. Parys, S.W. Sernett, S. DeLisle, P.M. Snyder, M.J. Walsh, and K.P. Campbell. Isolation, characterization, and localization of the inositol 1,4,5-trisphosphate receptor protein in Xenopus laevis oocytes. *J. Biol. Chem.*, 267:18776–18782, 1992.

[42] R. Payne, B. Walz, S. Levy, and A. Fein. The localization of calcium release by inositol trisphosphate in *limulus* receptors and its control by negative feedback. *Philos. Trans. R. Soc. London Ser. B*, 320:359–379, 1988.

[43] D.W. Peaceman and H.H. Rachford. The numerical solution of parabolic and elliptic differential equations. *Journal of the Society for Industrial and Applied Mathematics*, 3:28–41, 1955.

[44] J.W. Putney and G.J. Bird. The inositol phosphate-calcium signaling system in nonexcitable cells. *Endocrine Reviews*, 14(5):610–631, 1993.

[45] W.E. Schiesser. *Computational Mathematics in Engineering and Applied Science: ODE's , DAE's, PDE's.* CRC Press, Boca Rato, Fl, 1994.

[46] L.F. Shampine and M.W. Reichelt. The Matlab ODE Suite. Matlab Documentation.

[47] J.A. Sherratt. On the evolution of periodic plane waves in reaction-diffusion systems of $\lambda - \omega$ type. *Siam J. Appl. Math.*, 54(5):1374–1385, 1994.

[48] G.D. Smith. *Numerical Solution of Partial Differential Equations: Finite Difference Equations*, pages 110–113. Oxford University Press, Oxford University Press, New York, 3rd edition, 1989.

[49] A.J. Sneyd. Unpublished data.

[50] J. Sneyd, J. Keizer, and M.J. Sanderson. Mechanisms of calcium oscillations and waves: a quantitative analysis. *FASEB*, 9:1463–1472, November 1995.

[51] R. Somogyi and J.W. Stucki. Hormone-induced calcium oscillations in liver cells can be explained by a simple one-pool model. *J. Biol. Chem.*, 266:11068–11077, 1991.

[52] J.C. Strikwerda. *Finite Difference Schemes and Partial Differential Equations*, pages 142–153. Wadsworth and Brooks/Cole: Advanced Books and Software, Pacific Grove, California, 1989.

[53] R.W. Tsien and R.Y. Tsien. Calcium channels, stores, and oscillations. *Annu. Rev. Cell Biol.*, 6:715–760, 1990.

[54] P. Volpe, K-H Krause, S. Hashimoto, F. Zorzato, T. Pozzan, J. Meldolesi, and D.P. Lew. "Calciosome," a cytoplasmic organelle: the inositol 1,4,5-trisphosphate-sensitive $Ca^{2+}$ store of nonmuscle cells? *Proc Natl Acad Sci USA*, 85:1091–1095, 1988.

[55] M. Wakui, Y.V. Osipchuk, and O.H. Peterson. Pulsatile intracellular calcium release does not depend on fluctuations in inositol trisphosphate concentration. *Cell*, 339:317–320, 1989.

[56] N.K. Wessells and J.L. Hopson. *Biology*, pages 491–494. Random House, New York, 1988.

[57] N.K. Wessells and J.L. Hopson. *Biology*, pages 82–90. Random House, New York, 1988.

[58] N.K. Wessells and J.L. Hopson. *Biology*, page 84. Random House, New York, 1988.

[59] A.T. Winfree. *The Geometry of Biological Time*, pages 300–314. Springer-Verlag, 1980.

[60] A.T. Winfree. Vortices in motionless media. *Appl. Mech. Rev.*, 43:297–309, 1990.

[61] N.M. Woods, K.S.R. Cuthbertson, and P.H. Cobbold. Repetitive transient rises in cytoplasmic free calcium in hormone-stimulated hepatocytes. *Nature*, 319:600–602, February 1986.

[62] M. Wu and J. Gerhart. Raising Xenopus in the laboratory. In B.K. Kay and H.B. Peng, editors, *Xenopus laevis: Practical Uses in Cell and Molecular Biology*, volume 36 of *Methods in Cell Biology*, chapter 1, pages 3–18. Academic Press Inc., San Diego, California, 1991.

[63] Y.A. Yermakova and A.M. Pertosov. Interaction of rotating spiral waves with a boundary. *Biophysics*, 31:932–940, 1986.